geologica acta

Citation: Salehi Nejad, H., Shahosinie, E., Nazarinia, A., Lentz, D.R., 2024. Petrogenesis of the late Miocene Chenar volcanism in the southeast Urumieh-Dokhtar magmatic belt, Kerman, Iran: evidence from geochemical, U-Pb geochronologic, and Hf isotopic constraints. Geologica Acta, 22.1, 1-23 I-IV.

DOI: 10.1344/GeologicaActa2024.22.1

Petrogenesis of the late Miocene Chenar volcanism in the southeast Urumieh-Dokhtar magmatic belt, Kerman, Iran: evidence from geochemical, U-Pb geochronologic and Hf isotopic constraints

Hamideh Salehi Nejad[1] **Elham Shahosinie**[2] **Asma Nazarinia**[3] **David R Lentz**[4]

[1]**Department of Geology, Faculty of Sciences, Shahid Bahonar University of Kerman**
Pajoohesh Sq., Kerman 76169-14111, Iran E-mail: Hamideh.petrology@gmail.com Phone: 09137148319

[2]**Department of Geology, North Tehran Branch, Islamic Azad University**
Vafadar Blvd., Shahid Sadoughi St., Hakimiyeh Exit, Shahid Babaee Highway, Tehran, Iran.
E-mail: Elham_shahosinie@yahoo.com Phone: 09126315121

[3]**Department of Geology, Faculty of Sciences, University of Hormozgan**
KM 9 of Minab Road, Bandar Abbas, Iran. E-mail: A.Nazari.geo@gmail.com Phone: 09927994976

[4]**Department of Earth Sciences, University of New Brunswick**
PO Box 4400, 8 Bailey Drive, Fredericton, New Brunswick, Canada. E-mail: dlentz@unb.ca Department: 1-506-453-4804

ABSTRACT

The Chenar volcanic cone intruded the southeastern part of the Dehaj-Sarduiyeh volcano-sedimentary belt, in the southeast Urumieh-Dokhtar magmatic arc in Iran. The adakitic rocks, with porphyritic texture, mainly consist of rhyodacites and dacites, commonly comprised of phenocrysts of plagioclase, hornblende and biotite, with rare K-feldspar, in a groundmass composed of plagioclase, K-feldspar and quartz. They yielded U-Pb zircon ages of 5.52±0.099Ma, 5.46±0.12Ma, and 6.44±0.12Ma, and radiogenic εHf(t) values ranging from +3.1 to +12.7. The whole-rock geochemical analysis of these rocks reveals transitional calc-alkaline to shoshonitic characteristics.

The geochemical characteristics of the study rocks, particularly their high Sr/Y (~51.6-136.8) at low Y (~4.43–16.2ppm) and high La/Yb (~28.4–118.4ppm) at low Yb (~0.2–1.3ppm), are coherent with a high-silica adakitic signature. The whole-rock positive Eu/Eu^* anomaly and zircon Ce/Ce^* anomaly reflect the effects of an oxidized magmatic signature, with the rocks of the study area originating from a mantle source. The high- silica adakite geochemical characteristics of the Chenar volcanic cone support formation by partial melting of the modified mantle under the influence of metasomatized subducted oceanic slab in a post-collisional environment.

KEYWORDS **Urumieh-Dokhtar magmatic arc. Dehaj-Sarduiyeh volcano-sedimentary belt. Hf isotopes. U-Pb dating. Adakite. Iran.**

INTRODUCTION

Adakitic magmas can be generated in at least five ways: i) partial melting of oceanic crust (Defant and Drummond, 1990; Green and Harry, 1999; Kay, 1987); ii) slab break off in a post-collisional setting (Castillo, 2006, 2012); iii) melting of continental lower crust (Coldwell *et al.*, 2011); iv) slab window processes related to ridge subduction (Zhang *et al.*, 2010; Zhang and Zhai, 2012) and v) hydrous (involving amphibole) and/or high pressure (involving garnet) crystal fractionation of a mafic parent magma (Macpherson *et al.*, 2006; Muntener *et al.*, 2001; Moyen, 2009; Rossetti *et al.*, 2014). They are subdivided into Low-Silica Adakites (LSA; <60wt.% SiO_2) and High-Silica Adakites (HSA; >60wt.% SiO_2). The LSA are interpreted to be generated due to partial melting of the mantle wedge, whereas HSA are interpreted to be produced by partial melting of subducted oceanic crust (Martin *et al.*, 2005). A new type of adakite called 'continental' or C adakite has been described by Zhang *et al.* (2001) in East China, formed by partial melting of lower crust of garnet-amphibolite to eclogite facies.

Adakites are common along convergent plate margins (Castillo, 2006; Chiaradia *et al.*, 2009; Defant *et al.*, 2002; Kay and Kay, 2002; Yogodzinski and Kelemen, 1998) and this term is used to describe rocks of intermediate to felsic composition that have high Sr/Y ratios and notably low Heavy Rare Earth Elements (HREE) and Y values (Defant and Drummond, 1990; Zhang *et al.*, 2019).

Adakites are among a group of arc rocks that have recently received special attention in Iran. They have been reported in the northwest (Azizi *et al.*, 2014, 2019; Jamali and Mehrabi, 2015), in Central Iran (Ahmadian *et al.*, 2016; Delavari *et al.*, 2014; Omrani *et al.*, 2008), in the northeast (Mazhari, 2016; Omrani, 2018; Rossetti *et al.*, 2014; Shafahii Moghadam *et al.*, 2016) and along the Urumieh-Dokhtar Magmatic Arc (UDMA) (Ahmadian *et al.*, 2016; Asadi *et al.*, 2014; Mazhari, 2016).

Given the abundance of Fe^{3+} in the magma during partial melting, Cu^{-} and Au^{-} sulphides are oxidized by Fe^{3+} in the mantle wedge and the metals are released into the melts. The high-temperature and high-pressure fluids and/or melts are able to carry metals and the necessary ligands and thus accelerate mineralization. In contrast, some studies have proposed that adakitic slab melt is necessary for mineralization and it is commonly associated with high La/Yb and Sr/Y rocks. Experimental studies show that due to metasomatic reactions in the overlying mantle wedge, the contents of Cr, Ni and Mg increase significantly (Rapp *et al.*, 1999) during ascent through the mantle wedge.

Many researchers have described late Cenozoic adakite-like felsic rocks in the Kerman province and other parts of Iran (Omrani *et al.*, 2008; Pang *et al.*, 2016; Shaker Ardakani, 2016). They hypothesized that these rocks were produced due to the melting of the Neo-Tethyan slab beneath the collision zone (Omrani *et al.*, 2008) or the melting of the lower crust. Also, Kheirkhah *et al.* (2020) suggested that the igneous rocks from Dehaj-Sarduiyeh volcano-sedimentary belt, in the southeastern UDMA, belong to two distinct magmatic series. One series is entirely intrusive and of high-silica adakitic affinity and the other, comprising both hawaiite to trachyandesite lavas and intrusive rocks, is of high-K non-adakitic affinity.

The UDMA is part of the Zagros Orogenic Belt (ZOB), and it trends NW-SE, from eastern Turkey to southeast of Iran. It formed as a result of the northward subduction of Neotethyan oceanic crust underneath the Central Iran microcontinent. UDMA has been interpreted to be an Andean–type magmatic arc active from the late Jurassic to the Miocene with peak volcanism occurring in the middle to upper Eocene (Arvin *et al.*, 2007; Berberian and King, 1981). The youngest volcanic activity of UDMA was the formation of volcanic cones. Their composition is dacitic and rhyodacitic and belongs to the Mio-Pliocene. The cones intruded into a variety of rocks of Mesozoic to early Miocene age (Ghadami *et al.*, 2008). Ghadami and Nazarinia (2021) studied some granitoids in the northwest of Shahr-e-Babak and suggested they were adakitic (Kuh-Panj type) and that they formed by partial melting of a thickened, garnet-bearing, amphibolitic lower continental crust. Here, we report for the first time the occurrence of HSA in the UDMA, northwest of the Dehaj-Sardouyeh magmatic belt.

We present whole-rock geochemistry, zircon U-Pb ages, Hf isotopes and rare earth elements of zircon to constrain the petrogenesis of the Chenar volcanic cone. Our research shows evidence of Mio-Pliocene partial melting of modified mantle under the influence of a metasomatized subducted oceanic slab beneath the Central Iran.

GEOLOGY AND FIELD RELATIONSHIP

The Chenar Volcanic Cone (CVC) is located in the southeastern part of the UDMA (Fig. 1). Structurally, the studied area belongs to the tectonic range northwest of the Dehaj-Sardouyeh magmatic belt.

The UDMA forms a characteristic, linear, intrusive-extrusive complex (~150km width) that extends for 1700km parallel to the entire length of the Zagros orogenic belt. It consists of small to large plutonic bodies of granite, diorite and gabbro and, widely distributed, basaltic lava flows,

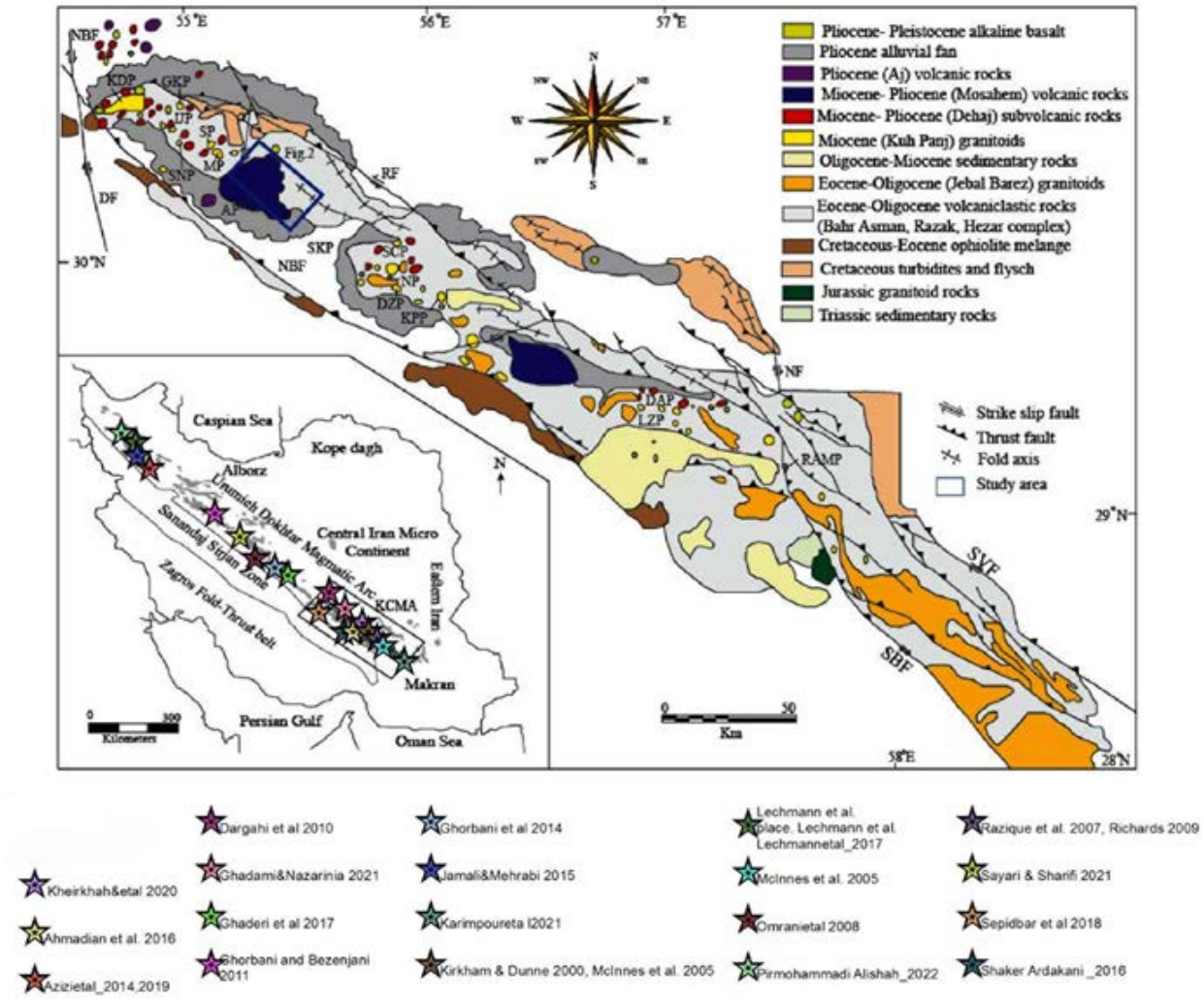

FIGURE 1. A) Simplified map of major structural units of Iran (modified after Alavi, 1996) showing location of the Dehaj-Sarduiyeh volcano-sedimentary belt in the Urumieh-Dokhtar magmatic arc (compiled from Dimitrijrvic, 1973; Emami *et al.*, 1993; Saric and Mijalkovic, 1973). B) Simplified geological map of the Dehaj-Sarduiyeh volcano-sedimentary belt and location of granitoids and sub-volcanic rocks (modified after Dimitrijrvic, 1973; Shafiei *et al.*, 2009).

trachybasalts (locally shoshonitic), andesite, dacite and trachyte, as well as ignimbrite and pyroclastic rocks (mostly tuff and agglomerate). The oldest known pluton in this assemblage is the calc-alkaline intrusion of Precambrian age exposed in the southeastern margin of Central Iran (Berberian and Berberian, 1981). The youngest rocks (mainly lava flows and pyroclastics) belong to Pliocene-Quaternary volcanic cones of alkaline and calc-alkaline composition. The Dehaj-Sardouyeh magmatic belt trends northwest-southeast and it is located in the southeastern part of the UDMA. Generally, this belt consists of voluminous intrusive and extrusive rocks mostly calc-alkaline in nature (Dimitrijevic, 1973).

In the Dehaj-Sardouyeh magmatic belt, there are numerous Mio-Pliocene sub-volcanic cones composed of dacite-andesite (Dimitrijevic, 1973). The last volcanic activity recorded in the belt took place in the Mio-Pliocene, which is divided into three groups: Dehaj, Mosahem and Aj types (Dimitrijevic, 1973). The CVC is Dehaj-type, and it is located east of the Mosahem (Fig. 2). The CVC intruded Eocene volcanic rocks (Fig. 3A). In the southern, western and northern parts of the cone, there are Eocene volcanic units (Thracian basalt, andesite and tuff), but in the eastern parts, there are more conglomerate and sandstone units (Dimitrijevic, 1973). The age of the emplacement of the sub-volcanic cones is Plio-Pleistocene according to Dimitrijevic (1973), while Moradian (1971) provided ages of 7-17Ma, based on K/Ar dating of 97 amphibole and biotite samples. Field studies indicate that the CVC is mainly comprised of light gray dacite rocks with porphyry textures (Fig. 3B). The most important phenocrysts are plagioclase, amphibole, biotite and local quartz. Plagioclase is the most abundant and sometimes comprises half of the rock volume.

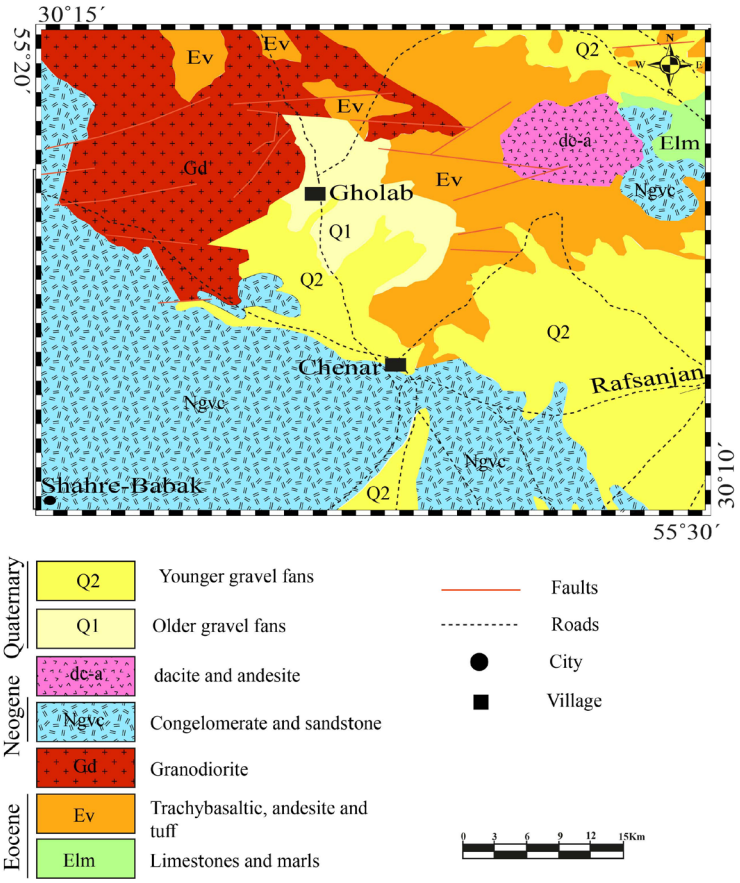

FIGURE 2. Simplified geological map of the Chenar Volcanic Cone (modified after Dimitrijrvic, 1973).

PETROGRAPHY

The CVC rocks consist of dacite and rhyodacite. They show porphyritic texture with phenocrysts of plagioclase, hornblende and biotite, with K-feldspar in a groundmass together with plagioclase, and quartz (Fig. 4A). Plagioclase is the most abundant phenocryst (25-50vol %) and contains inclusions of amphibole and opaques. Dacites contain large plagioclase phenocrysts (3-5mm) that usually exhibit sieve textures (Fig. 4B). In some samples, plagioclase crystals have inclusion-rich cores. Hornblende occurs as the main ferromagnesian phenocryst (up to 2mm) in dacite and varies from green to brown in color. Hornblende crystals are sometimes altered to chlorite and calcite (Fig. 4C). Hornblende is often altered, changing to an assemblage dominated by Fe-Ti oxides. In some samples, the accumulation of hornblende led to the formation of glomeroporphyritic texture. The groundmass is composed of plagioclase and hornblende as the main minerals, with apatite, biotite, quartz and iron oxides as accessory minerals.

Rhyodacite is less common than dacite in the study area. In rhyodacites quartz is generally fine to medium sized and appears as anhedral to subhedral crystals (Fig. 4D). The feldspar, with micro-inclusions of magnetite, zircon, titanite and apatite, occurs as anhedral crystals. Biotite forms individual phenocrysts and is fine-grained, locally deformed and altered to chlorite. Accessory minerals include Fe-Ti oxides, carbonate, apatite, zircon and titanite.

ANALYTICAL METHODS

A total of 50 samples from the CVC were collected for petrographic and whole-rock geochemical and isotopic studies. Zircons were separated from samples CHE-2, CHE-3 and CHE-7 using standard crushing, heavy liquid and isodynamic separation techniques at the Geological Survey of Iran. Cathodoluminescence (CL) images were acquired to characterize the internal structures of zircons to choose appropriate sites for U-Pb analyses. For LA-ICP-MS zircon U-Pb analysis, zircons were separated following electrostatic disaggregation (self-rag) of the rock sample, using standard gravimetric and magnetic techniques; grains were picked under a binocular microscope and mounted in epoxy discs. All grains were imaged by CL

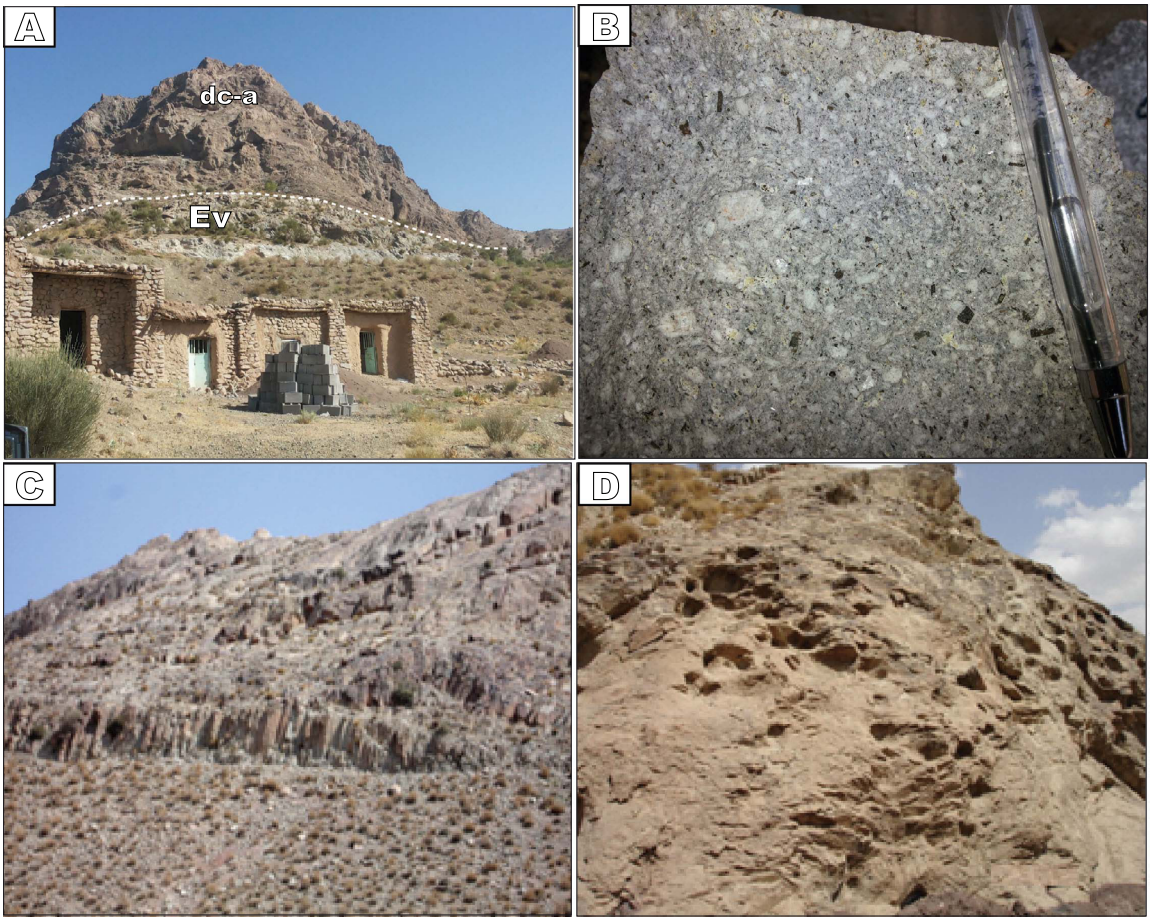

FIGURE 3. A) The Chenar Volcanic Cone (CVC; dc-a unit, dacite rocks) intruded into Eocene volcanic rocks (Ev unit, trachybasalt, andesite and tuff rocks). B) Porphyritic texture in dacite from the CVC. C) Tectonic joints in the Chenar Volcanic Cone. D) Tafoni cavities in the CVC.

and BSE (BackScattered Electron) to provide maps to guide the choice of analytical spots. The discs were coated with carbon for analysis. Zircon U-Pb ages were obtained using a 193nm ArF EXCIMER laser with an Agilent 7700 ICP-MS system in the Geochemical Analysis Unit of the ARC Centre of Excellence for Core to Crust Fluid Systems (CCFS/GEMOC) Macquarie University, Australia; detailed method descriptions have been presented by Jackson *et al.* (2004). The ablation conditions included beam size (30μm), pulse rate (5Hz) and energy density (7.59J/cm^2). Analytical runs comprised 16 analyses with 12 analyses of unknowns bracketed by two analyses of a standard zircon GJ-1 at the beginning and end of each run, using the established TIMS values (^{207}Pb/^{206}Pb age= 608.5Ma; Jackson *et al.*, 2004). Supplementary Table I, Appendix and Table 1 presents the detailed results of zircon U-Pb geochronology analyses of the CHE-2, CHE-3 and CHE-7.

Zircon Hf-isotope analyses were performed on the same zircon grains that were subjected to U-Pb dating at Macquarie University using a Thermo Scientific Neptune (Plus) multiple collector–ICP–MS (MC–ICP–MS) coupled to a New Wave 213nm solid-state laser ablation system (Table II, Appendix). The laser ablation beam was 40 or 55μm in diameter and used a 10Hz laser repetition rate and a laser energy of 10–11J/cm^2. Ablated material was injected into the MC–ICP– MS with a high-purity He carrier gas. Details of the instrumental conditions and data acquisition protocols are given by Wu *et al.* (2006). The ^{176}Hf/^{177}Hf ratio was normalized to ^{179}Hf/^{177}Hf = 0.7325. Hafnium isotopic data were age-corrected using a ^{176}Lu decay constant of 1.867 × 10^{-11} a– 1 (Soderlund *et al.*, 2004). εHf(t) values and Hf model ages were calculated using the methods of Bouvier *et al.* (2008) and Griffin *et al.* (2002), respectively.

For whole-rock geochemistry, 10 samples of the CVC with minimal alteration were selected and powdered in Damghan University mining-lab and then they were sent to ACME Lab in Vancouver, Canada for whole-rock chemical analysis (Table 2). Major elements were analyzed using fusion X-Ray Fluorescence spectrometry (XRF), and fusion Inductively Coupled Plasma-Mass Spectrometry (ICP-MS). For XRF, detection limits were

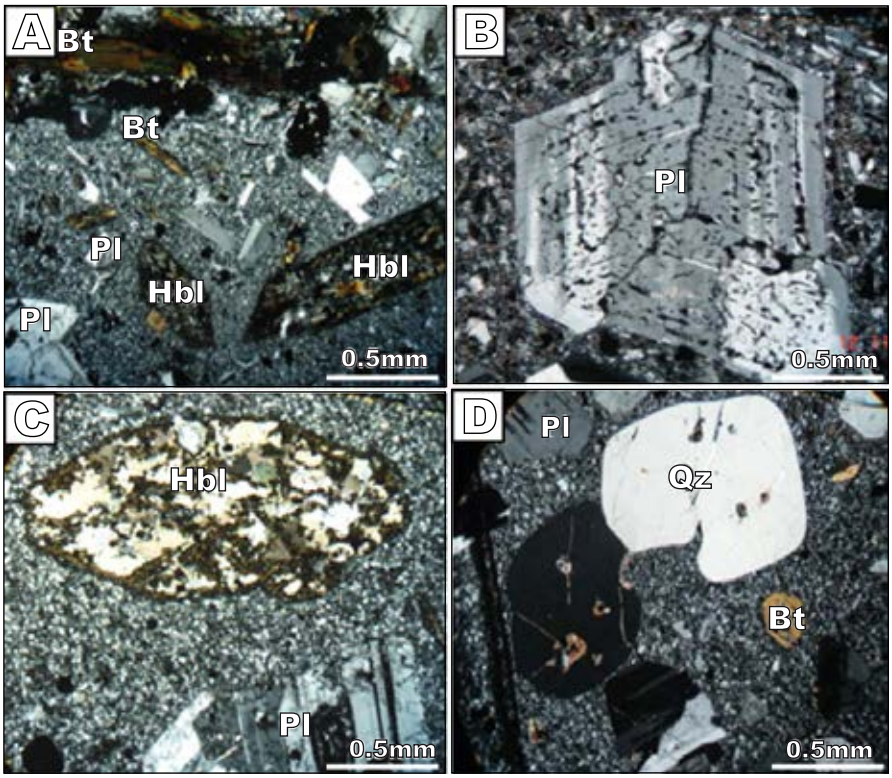

FIGURE 4. Representative cross polarized light photomicrographs of dacite and rhyodacite from the study area rocks. A) Porphyritic texture in dacite, B) Plagioclase exhibiting sieve texture. C) Hornblende altered to chlorite and calcite. D) Anhedral quartz crystals in rhyodacite. Abbreviations: Pl= Plagioclase, Hbl= hornblende, Bt= biotite, Qz= quartz (abbreviation based on Whitney and Evans, 2010).

reported as percentages (%) for major oxides and parts-per-million (ppm) for trace elements. Refractory and Rare Earth Elements (REEs) were carried out using lithium fusion and ICP-MS of powdered samples (0.2g), following a $LiBO_2/Li_2B_4O_7$ fusion and nitric acid total digestion (LF 100), at ACME Laboratories, Vancouver, Canada. This method offers increased sensitivity for 31 elements including REEs and trace elements occurring at low concentration levels (Cs, Ta, Th, U, Hf), with detection limits of around 0.01ppm. In LF100-ICP-MS analysis, Detection Limits (DLs) change for REEs from 0.01ppm (Tb, Tm, and Lu) to 0.3ppm (Nd) and for other trace elements from 0.1ppm (Rb, Zr, Nb, Y, Cs, Ta, Hf, and U) to 8ppm (V).

RESULTS

U-Pb geochronology

LA-ICP-MS analytical results of U-Pb on zircons from CVC (CHE-2, CHE-3 and CHE-7) are listed in Table I, Appendix. The uranium (CHE-2=556-3891ppm; CHE-3=369-4533ppm; CHE-7=167-3841ppm) and thorium (CHE-2=320-9808ppm; CHE-3=180-23022ppm; CHE-7=56-4712ppm) concentrations and high Th/U ratios (CHE-2=0.5-2.5; CHE-3=0.4-5.07ppm; CHE-7=0.3-1.2ppm) in zircons show their magmatic origin (Belousova *et al.*, 2002; Kirkland, 2015).

Concordia diagrams of thezircons from the CVC (CHE-2, CHE-3 and CHE-7) are shown in Figure 5. Reduction of the data shows an age of 5.52±0.099Ma Mean Squared Weighted Deviation (MSWD= 2) for CHE-2, 5.46±0.12Ma (MSWD= 3.1) for CHE-3, and 6.44±0.12Ma (MSWD= 1.5) for CHE-7 (Fig. 5A-C). These results indicate that the CVC formed in the late Miocene. All zircon grains from the CVC are euhedral to subhedral and CL images show that most of them exhibit oscillatory zoning (Fig. 6A-B).

The results of REE for zircons from the CVC (CHE-7) are presented in Table 1. Chondrite normalized plot of REE shows a steeply increasing slope from Light Rare Earth Elements (LREE) to HREE, a positive Ce anomaly (Ce/Ce^*= 1.6-36.6) and positive Eu anomaly (Eu/Eu^*= 1.01-2.5) (Fig. 5D). These characteristics probably indicate relatively oxidizing conditions for the CVC parental magma (*e.g.* Guo *et al.*, 1996; Hoskin and Schaltegger, 2003). Moreover, the general REE pattern is characteristic of unaltered igneous zircon (Hoskin and Schaltegger, 2003).

TABLE 1. Rare earth element data (in ppm) for zircons from the Chenar area (sample CHE-7)

Sample	La	Ce	Pr	Nd	Sm	Eu	Gd	Dy	Ho	Er	Yb	Lu
CHE7-01	1.511	7.650	2.040	2.820	9.730	9.100	33.750	125.820	227.080	402.430	1251.470	1526.930
CHE7-02	0.266	33.560	3.030	9.880	55.260	63.650	160.400	431.360	665.580	1004.570	2446.270	2571.760
CHE7-03	0.587	4.970	0.618	1.568	9.740	7.440	42.840	169.270	311.460	541.030	1590.270	1908.790
CHE7-04	2.105	62.070	2.820	5.770	24.800	25.930	80.600	214.950	339.210	513.070	1246.190	1363.860
CHE7-05	0.462	122.730	6.670	22.990	98.660	122.420	262.330	614.120	898.910	1269.790	2731.680	2866.310
CHE7-06	0.017	8.420	0.292	0.931	6.640	10.770	28.780	106.480	193.660	332.240	994.040	1199.040
CHE7-07	8.590	49.960	5.180	5.380	14.060	14.600	54.210	173.480	293.150	476.780	1282.390	1504.990
CHE7-08	0.791	4.910	0.898	1.644	9.130	7.930	36.190	146.320	274.360	485.410	1528.260	1893.310
CHE7-09	1.182	4.410	0.937	1.297	5.120	4.710	22.530	92.390	173.930	315.600	995.980	1267.630
CHE7-10	0.145	54.350	3.840	11.480	58.500	71.880	181.710	563.060	928.680	1487.730	3769.060	4141.570
CHE7-11	0.742	115.860	1.830	6.210	44.870	44.490	208.390	717.570	1193.870	1834.500	4243.540	4330.220
CHE7-12	0.031	22.180	0.428	1.443	10.690	16.960	48.050	143.080	229.330	347.860	870.260	990.400
CHE7-13	0.348	22.320	0.841	2.520	12.540	14.490	43.530	134.930	231.760	389.990	1107.320	1315.420
CHE7-14	-0.002	4.130	0.180	0.486	4.280	7.330	18.700	71.520	121.740	201.130	564.620	669.050
CHE7-15	0.038	24.670	1.176	4.340	24.630	32.290	89.880	304.360	526.550	878.050	2349.630	2667.690
CHE7-16	0.017	7.740	0.242	0.922	5.810	9.830	25.470	97.020	174.690	299.840	890.950	1087.990
CHE7-17	0.295	37.480	3.680	10.540	53.030	68.780	159.890	448.140	707.110	1087.550	2586.000	2835.460
CHE7-18	0.030	6.210	0.217	0.873	6.380	6.410	33.680	154.600	297.680	540.770	1642.330	1999.190
CHE7-19	0.811	63.570	5.160	14.740	73.820	94.330	244.740	655.450	1015.580	1469.780	3298.640	3510.510
CHE7-20	0.280	12.170	0.718	1.520	10.530	7.460	48.160	192.080	350.660	613.980	1854.160	2146.610
CHE7-21	0.041	17.190	1.189	3.910	19.460	26.860	67.140	228.090	407.290	682.440	1887.700	2304.660
CHE7-22	0.130	19.110	0.195	0.682	4.640	6.050	23.930	96.580	179.120	314.340	938.430	1166.310
CHE7-23	-0.001	4.520	0.210	0.652	4.710	8.120	21.440	79.240	141.770	232.760	618.520	760.760
CHE7-24	0.017	17.690	0.469	1.512	9.670	13.900	50.440	207.770	367.160	606.200	1613.060	1868.100
CHE7-25	0.345	22.770	2.200	6.280	33.830	39.080	109.320	298.020	473.800	745.860	1912.140	2112.780

Zircon Hf isotope

Fifty-six dated zircons from CVC samples CHE-2, CHE-3 and CHE-7 were analyzed for Hf isotopes (Table II, Appendix; Fig. 6). Fifteen analyses of zircons from sample CHE-2 gave $^{176}Hf/^{177}Hf$ values of 0.282994–0.283068. These analyses correspond to εHf(t) values of +7.9 to +10.5 and yield Hf crustal model ages (T^{C}_{DM}) of 412–579Ma. $^{176}Hf/^{177}Hf$ values of fifteen zircons from sample CHE-3 range between 0.283003 and 0.283077, and yield positive εHf(t) values from +8.2 to +10.9 and Hf crustal model ages (T^{C}_{DM}) of 391–559Ma. Fifteen analyses of zircons from sample CHE-7 gave $^{176}Hf/^{177}Hf$ values of 0.282858–0.283124, yielding εHf (t) values of +3.1 to +12.7 and Hf crustal model ages (T^{C}_{DM}) of 280 to 886Ma.

Zircon Hf isotope data have been used increasingly to constrain global models for the growth and differentiation of the continental crust (Amelin *et al.*, 2000; Belousova *et al.*, 2010; Corfu and Noble, 1992; Dhuime *et al.*, 2012; Harrison *et al.*, 2005; Hawkesworth *et al.*, 2010; Iizuka *et al.*, 2010; Kemp *et al.*, 2006; Kemp and Hawkesworth, 2013; Patchett, 1983; Stevenson and Patchett, 1990; Vervoort *et al.*, 1996). Based on various studies, the value of εHf in the old subcontinental enriched asthenosphere mantleis negative (-12 to -30) (Griffin *et al.*, 2000). Positive, but low Hf values (from 0 to 5) indicate crustal contamination or the presence of xenocrystic zircon. While positive and high Hf values indicate root magma from the mantle without crustal contamination (Corfu and Scott, 1993; Patchett *et al.*, 1981, 1993). The studied samples from the CVC are in the range of mantle.

Continental crust components such as mature sands generally have high abundance of zircon and thus, have super-chondritic Hf/Sm ratios, whereas pelagic sediments and marine pelites, which contain relatively few zircons, are characterized by much lower Hf/Sm ratios because zircon is Hf-enriched and LREE-depleted (Hoskin and Schaltegger, 2003; Prelevic *et al.*, 2012). The upper continental crustal sediments, which might contain a higher proportion of zircon-rich coarse sands, are characterized by higher Hf content and lower Lu/Hf ratios (Sun *et al.*, 2018). The isotopic composition of Hf is not affected by changes in physical conditions or crystallization path. However chemical and morphological changes during zircon growth cause changes in Hf isotopic composition. Various mechanisms such as wall-rock reaction, restite segregation or magma mixing must be considered. For this purpose, the chemistry of zircon should be studied in detail.

TABLE 2. Whole-rock geochemical compositions of representative samples of the Chenar area

Sample	CHE-8	CHE-2	CHE-3	CHE-6	CHE-7	CHE-1	CHE-4	CHE-5	CHE-9	CHE-10
Location	Chenar	Chenar	Chenar	Chenar	Chenar	Chenar	Chenar	Chenar	Chenar	Chenar
(wt%)										
SiO_2	71.12	66.69	67.14	66.36	64.93	67.67	67.19	70.15	65.43	68.67
TiO_2	0.27	0.40	0.42	0.43	0.48	0.41	0.43	0.27	0.44	0.33
Al_2O_3	16.06	17.04	17.03	16.66	17.24	16.98	17.17	16.08	16.24	17.98
FeO_{tot}	1.81	2.82	2.99	2.86	3.51	2.91	2.91	1.81	2.51	1.71
MnO	0.02	0.05	0.06	0.05	0.06	0.05	0.05	0.02	0.06	0.06
MgO	0.49	0.96	0.91	0.95	1.22	0.85	0.91	0.45	1.53	0.95
CaO	2.50	3.46	3.31	4.04	4.16	3.02	3.22	2.60	4.08	4.24
Na_2O	4.66	5.15	5.09	5.29	4.65	5.23	5.07	4.26	5.75	4.23
K_2O	3.36	3.06	3.10	3.07	2.50	3.14	3.02	3.39	3.67	3.28
P_2O_5	0.11	0.24	0.26	0.23	0.25	0.22	0.24	0.20	0.23	0.33
LOI	0.00	0.04	0.02	0.02	0.01	0.02	0.04	0.30	0.02	0.02
Total	100.4	99.9	100.3	99.9	99.0	100.4	100.2	99.5	99.9	101.7
(ppm)										
Co	2.27	5.68	6.57	6.11	6.65	5.68	6.04	2.27	5.65	5.66
Ni	1.45	7.58	8.54	7.32	8.37	6.72	7.59	1.45	7.47	6.12
Cu	23.6	33.4	37.1	26.3	29.3	30.2	34.6	23.6	30.3	31.2
Zn	38.1	51.9	59.0	53.4	58.9	54.1	53.5	38.1	51.0	52.1
Cs	2.44	2.17	1.89	3.34	3.05	2.43	1.66	2.44	2.05	2.16
Rb	87.2	75.8	81.2	74.2	66.0	77.5	75.8	87.2	76.0	78.5
Ba	809.0	859.5	931.3	879.3	740.1	855.7	848.8	809.0	733.1	800.7
Th	13.29	10.55	10.69	9.30	5.66	10.14	9.66	13.19	7.66	9.14
U	3.93	3.16	3.19	2.86	2.34	3.18	2.90	3.83	3.34	2.18
Nb	5.11	8.15	8.93	8.15	6.95	8.22	7.98	5.11	7.95	7.22
Ta	0.41	0.53	0.61	0.52	0.55	0.54	0.51	0.39	0.45	0.44
La	33.38	39.15	41.25	36.27	20.43	35.84	36.36	33.38	28.43	38.84
Ce	57.33	69.82	76.92	66.48	39.92	65.23	66.28	57.33	49.92	66.23
Pb	20.34	18.04	19.44	17.96	16.08	17.51	18.57	20.34	18.08	18.51
Pr	6.35	7.99	8.81	7.70	5.34	7.67	7.81	6.35	6.34	7.17
Sr	605.60	857.50	898.80	866.20	838.10	800.50	819.00	605.60	822.10	805.50
Nd	22.18	28.56	32.13	27.87	21.85	27.84	28.48	22.18	22.85	27.90
Zr	76.1	116.0	158.2	94.5	80.2	119.1	145.2	76.1	82.2	118.1
Sm	3.23	4.35	5.00	4.30	4.30	4.32	4.44	3.23	3.30	3.32
Eu	0.90	1.20	1.34	1.16	1.17	1.16	1.20	0.90	1.66	1.29
Dy	0.98	1.55	1.76	1.53	2.61	1.52	1.55	0.98	2.19	1.18
Y	4.43	7.82	8.40	7.41	16.23	7.56	7.54	4.43	11.23	6.56
Yb	0.28	0.55	0.61	0.53	1.37	0.53	0.54	0.30	1.00	0.47
Lu	0.04	0.09	0.10	0.08	0.23	0.09	0.09	0.05	0.23	0.10
Sc	2.15	3.74	4.34	3.76	5.58	3.85	3.74	2.15	4.58	3.85
V	24.6	41.7	52.4	51.8	65.1	43.4	48.2	25.6	6115.0	45.4
Cr	2.56	8.46	10.03	8.85	7.19	7.81	9.58	2.96	8.19	6.81

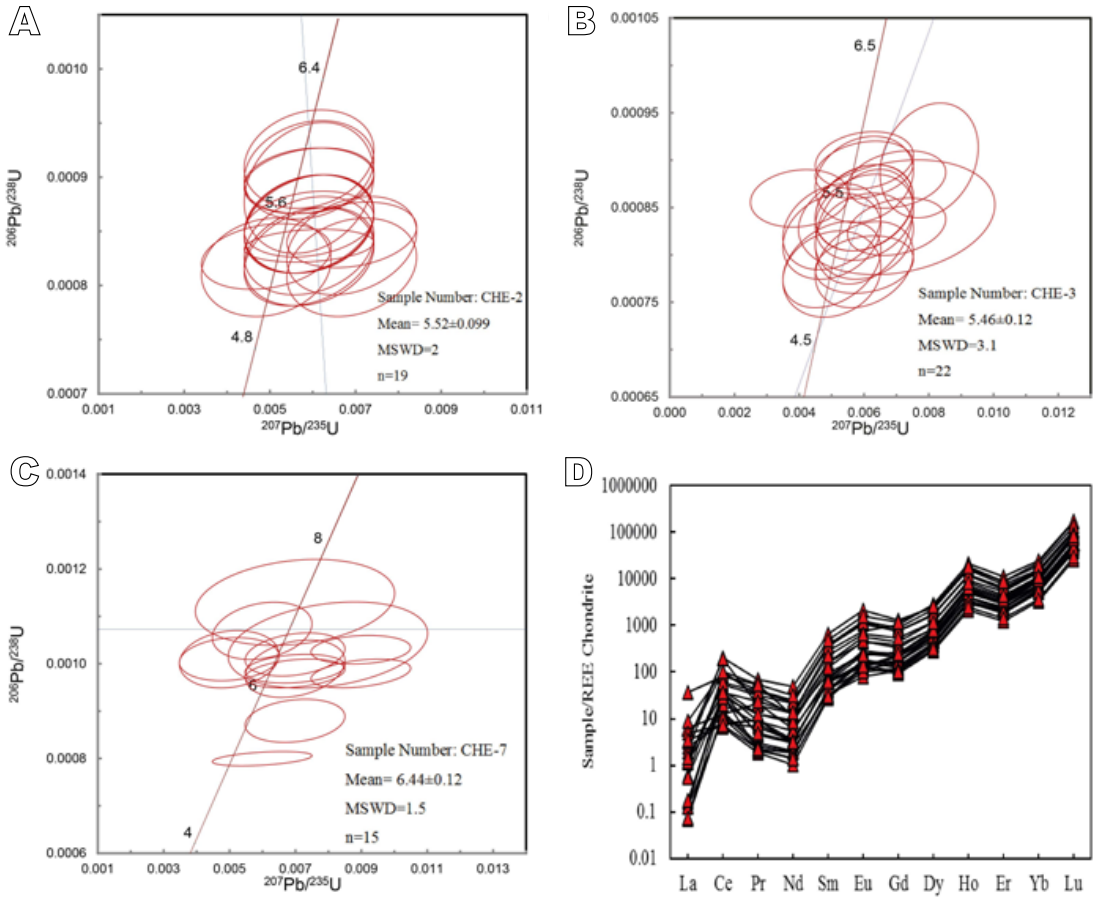

FIGURE 5. The Laser ablation inductively coupled plasma-mass spectrometry (LA-ICP-MS) U-Pb zircon concordia diagrams for the for A) CHE-2, B) CHE-3 and C) CHE-7; D) Diagrams of chondrite-normalized REE patterns for zircons(sample CHE-7) and chondrite values are from Sun and McDonough (1989).

Whole-rock geochemistry

The results of the whole-rock composition of the CVC are listed in Table 2. The Loss On Ignition (LOI) value for all samples is less than 0.3wt%, showing negligible alteration. In the immobile element chemical classification diagram of Winchester and Floyd (1977), the samples from the CVC plot in the field of rhyodacite and dacite (Fig. 7A). The calc-alkaline to shoshonitic nature of the CVC is also clear on the Th versus Co diagram (Fig. 7B). These rocks contain 64.9–71.1wt% SiO_2 and 16.06–17.97wt% Al_2O_3, with an average Mg# of 26.04 (MgO < 1.6wt%). They have relatively low concentrations of Ni (1.5-8.5ppm), Cr (2.56-10.03ppm) and Sc (2.15-5.58ppm). Concentration of Sr is relatively high, ranging from 605.6 to 898.8ppm, whereas concentrations of Y are rather low at the level of several ppm.

Most samples from the CVC have similar chondrite-normalized REE patterns, which exhibit high LREE and quite low HREE and a negative trend from the LREE to HREE (Fig. 8A; Table 2). They show key positive Eu anomalies (Fig. 8A) (Eu/Eu^*= 1.01-1.70), with only one sample (CHE-7) showing a negative Eu anomaly (Eu/Eu^*= 0.89). On primitive mantle-normalized trace element diagrams, the CVC form rather parallel patterns (Fig. 8B), with relative enrichment in some Large Ion Lithophile Elements (LILE; Cs, Sr, K and Pb) and depletion in Nb, Ti and Ta. The pattern is characteristic of continental crust rocks (Rudnick and Gao, 2014) and subduction-related magmas (Pearce and Peate, 1995).

In Harker diagrams all compatible elements negatively correlate; cobalt, V, Ni and certain REEs (Eu, Yb and Lu) contents decrease with increasing SiO_2 (Fig. 9). K_2O and several other highly incompatible trace elements exhibit positive correlations with SiO_2 with some scattering, possibly due to alteration. Potassic metasomatism, the presence of muscovite and biotite and sometimes potassium enclaves like alkali syenite are the cause for high K_2O content.

All samples display geochemical features of adakites, including high Sr/Y (~51.6-136.8) at low Y (~4.43–

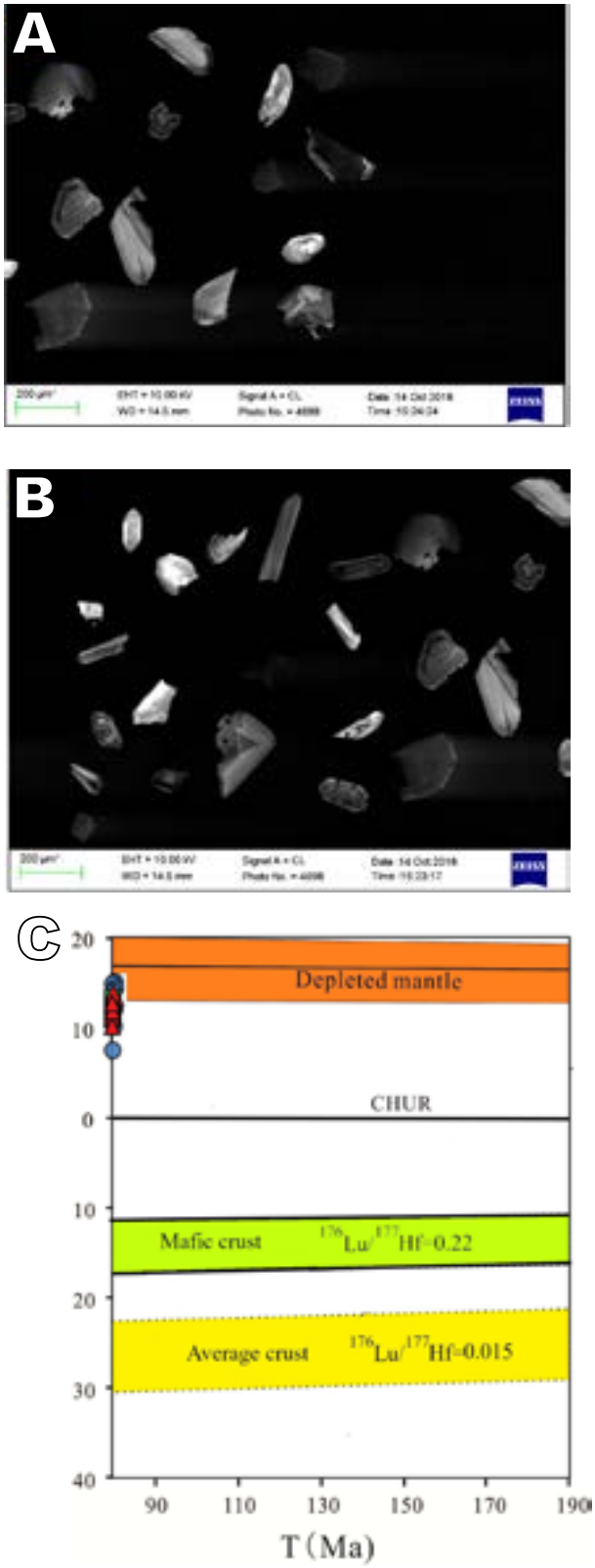

FIGURE 6. A, B) CL images of zircons. C) Plot of εHf(t) values versus T(Ma) ages of zircons from Chenar volcanic rocks (Griffin *et al.*, 2004).

16.2ppm) and high La/Yb (~28.4-118.4) at very low Yb (~0.2-1.3ppm). Furthermore, all of them plot within the adakite field in Sr/Y versus Y and $(La/Yb)_N$ versus $(Yb)_N$ diagrams (Fig. 10A-B).

DISCUSSION

Petrogenesis of CVC

The CVC exhibits typical geochemical signatures of subduction-related magmas. This is supported by enrichment of LILEs and LREEs over HFSEs, negative Nb-Ta and Ti anomalies in the primitive mantle-normalized spider diagrams (Fig. 8A-B; Kogiso *et al.*, 1997; Imer *et al.*, 2014; Ozdemir, 2011). The subparallel chondrite-normalized REE patterns (Fig. 8A) and the notable similarities between the primitive mantle-normalized spider diagram patterns (Fig. 8B) for CVC may provide further confirmation that CVC are co-magmatic. The positive Eu anomalies in the samples of the CVC could be explained by oxidizing conditions in their primary magmas (Richards *et al.*, 2001). In addition, the negative correlation between MgO, FeO, Al_2O_3, CaO, TiO_2 and SiO_2 (Fig. 9) are attributed to the fractionation of plagioclase, hornblende, apatite and titanite.

The geochemical characteristics of the CVC, namely their SiO_2 (av. 67.53wt%), MgO (av. 0.92wt%), Al_2O_3 (av. 16.84wt%), low Y (av. 8.16ppm) content, high Sr content (av. 791ppm), Sr/Y>20 (av. 106.93) and positive Eu anomaly (Eu/Eu^*= 1.01-1.70), all indicate their similarity with those of adakitic magmatic rocks (Defant and Drummond, 1990; Martin *et al.*, 2005; Richards and Kerrich, 2007). Source characteristics, oxygen fugacity (fO_2) of magmatic systems, and the Plagioclase /mafic state ratio of minerals affect the Eu anomaly in the melt (Fang and Sheng, 2010). Furthermore, the adakitic affinity of the CVC is also presented in Sr/Y versus Y and $(La/Yb)_N$ versus $(Yb)_N$ diagrams (Defant and Drummond, 1990; Fig. 10A-B). According to the classification scheme of Martin *et al.* (2005), the CVC belongs to HSA (Fig. 10C-D). The continental crust is too thick. Only if pressure >1.8GPa (~60km), low grade Melting of dry mafic eclogite can produce dacite melt K_2O/Na_2O ~1 because garnet controls the composition of molten SiO_2. However, at pressure <1.8GPa, the presence of abundant plagioclase in the remaining phases leads to a melt with lower SiO_2 than that of C-type adakites (Fang and Sheng, 2010). If the depth is lower than 60km, regardless of the melting degree, the mafic lower continental crust cannot produce melts with high SiO_2 and high K_2O/Na_2O. The additional heat source from the rising mantle in the extensional tectonic environment provides the necessary heat to melt the lower mafic continental crust (Fang and Sheng, 2010).

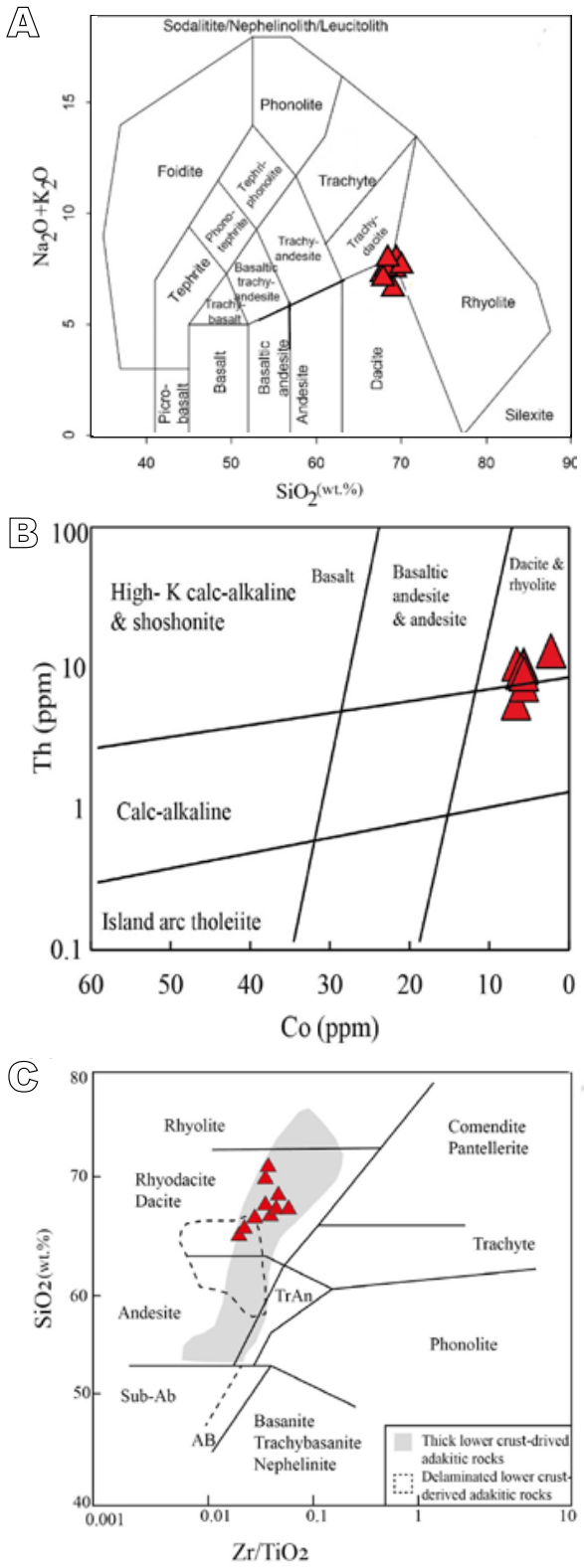

FIGURE 7. A) Na_2O+K_2O versus SiO_2 plot (Midelmost, 1985). B) Th versus Co plot (Hastie *et al.*, 2007). C) Zr/TiO_2 vs. SiO_2 (Winchester and Floyd, 1977); Gray and dotted areas are compiled from Gao *et al.* (2004), Guan *et al.* (2012), Jiang *et al.* (2011), Lei (2016), Li *et al.* (2013), Li *et al.* (2014), Liu *et al.* (2015), Lv *et al.* (2011), Ma (2013), Ma and Yue (2010), Sun *et al.* (2015), Wang *et al.* (2014), Yu *et al.* (2011), Zhang *et al.* (2014).

The High Sr/Y ratio (~51.6-136.8) indicates incorporation of plagioclase in the melting process, as plagioclase becomes unstable by pressure increase and consequently, Sr is released. On the other hand, remaining garnet as a residual phase in the source region or garnet differentiation from magma at deep levels can be responsible for the low Y content and high Sr/Y ratio (Moyen, 2009). Moreover, Low Silica Adakites (LSAs) have higher Sr/Y and La/Yb ratios and is characterized by more differentiated REE pattern compared to HSAs. According to the above, the Sr/Y and La/Yb ratios (51.6-136.7 and 28.4-118.4 respectively) and the REE pattern of the CVC do not correspond to low-silica adakites.

Richards and Kerrich (2007) assert that major part of the differentiated calc-alkaline magmas display false adakitic characteristics, owing to the differentiation of

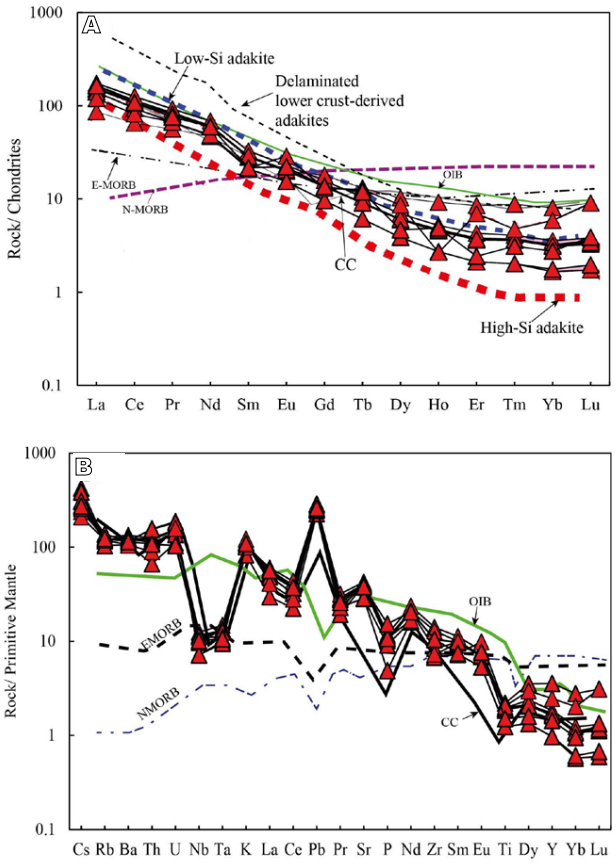

FIGURE 8. A) Chondrite-normalized Rare Earth Element (REE) patterns (Sun and McDonough, 1989). Average values of low-SiO_2 and high-SiO_2 adakite are from Martin *et al.* (2005). B) Primitive mantle-normalized multielement spider diagram (Sun and McDonough, 1989). For comparison, patterns of average Continental Crust (CC; Rudnick and Gao, 2014) and Ocean Island Basalt (OIB; McDonough and Sun, 1995) are also shown. E-MORB and N-MORB trends are from Sun and McDonough (1989). Fields for delaminated lower-crust-derived adakites and thick lower-crust-derived adakites are from Karsli *et al.* (2019).

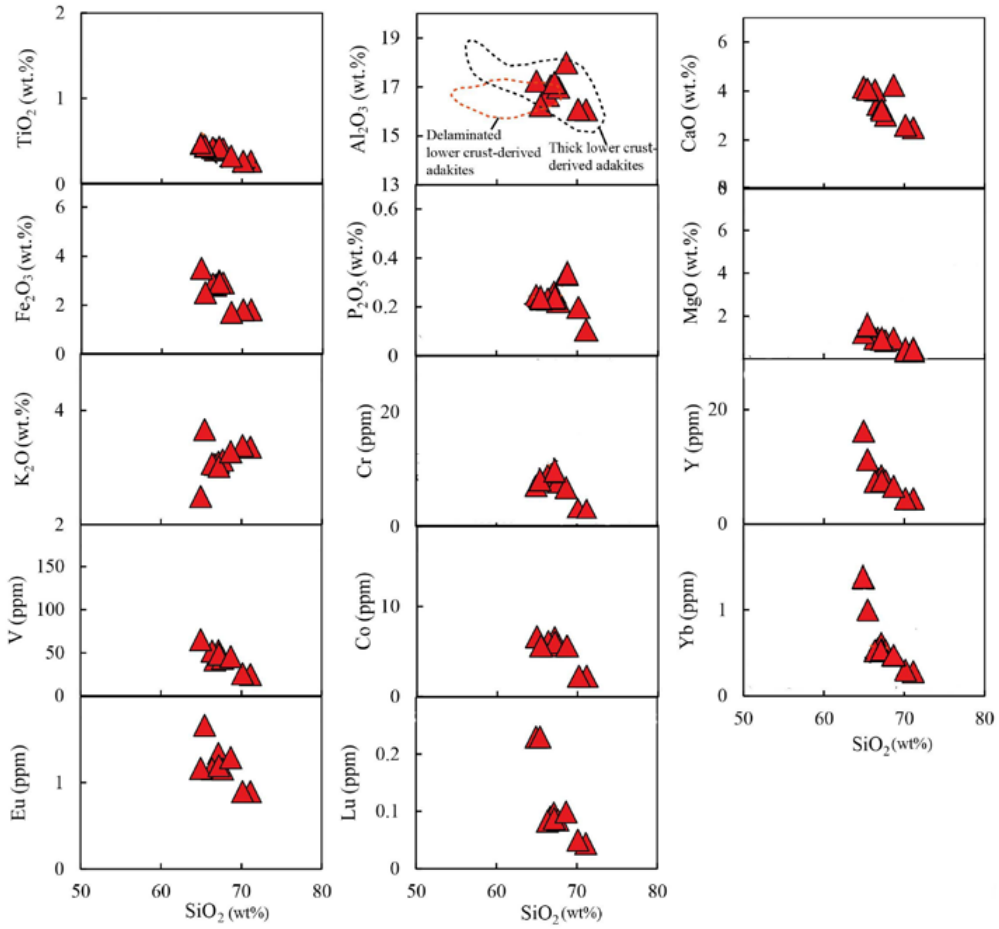

FIGURE 9. Harker diagrams of selected major oxides and trace elements for Chenar Volcanic Cone (CVC).

garnet and amphibole and a decrease in Y and HREE. However, the Sr/Y ratio in the CVC is higher than the La/Yb ratio and so, based on Richards and Kerrich (2007), they can be considered as real adakites. Furthermore, they believe that adakitic natures such as low Y and Yb values and high Sr/Y and La/Yb ratios can also be related to fractional crystallization or partial melting (Richards and Kerrich, 2007). Based on La/Yb vs. La diagram (Fig. 11A), the compositional trend of the CVC corresponds well to the partial melting, rather than fractional crystallization. Moreover, the data point trend in the Ba/Nb vs. Nb diagram (Fig. 11B) also testifies to the occurrence of partial melting (Bourdon *et al.*, 2002). Thus, the CVC share substantial similarities with High Silica Adakites (HAS), as their SiO_2 value is generally higher than 64% and their Yb/Lu ratio is 4.3 to 7, they have similar range of SiO_2 compared to the high-silica (Martin *et al.*, 2005).

Estimating the effect of alteration is essential before using geochemistry of rocks to infer high temperature magmatic processes. Aftabi and Atapour (2009) proposed that secondary loss of Y might lead to incorrect classification for some Iranian 'adakites' (Omrani *et al.*, 2008, 2009). Here, all studied rocks have LOI lower than 0.3wt.% (Table 2) and the values are not correlated with abundances of fluid-mobile element such as LILE, an observation not to be expected if alteration exerts control on both. Also, the coherent REE and spider patterns of the CVC (Fig. 8A-B) and the petrographic descriptions noted in an earlier section argue against significant alteration.

The adakitic rocks could be formed by different processes including: i) low degree partial melting of metasomatized mantle (Gao *et al.*, 2010; Jiang *et al.*, 2006; Pearce and Peate, 1995); ii)partial melting of subducted slab under eclogite facies conditions (Defant and Drummond, 1990); iii) partial melting of over thickened and delaminated mafic lower crust (Castillo *et al.*, 1999; Robin *et al.*, 2009) and iv) magma mixing between basaltic magmas and felsic melts derived from continental crust (Guo *et al.*, 2007). Partial melting of the subducted oceanic crust typically generates adakitic magma with high Si, Al, Sr (>400ppm) and Sr/Y (>20) and low Y (<20) and depleted Sr–Nd isotopic composition ($^{87}Sr/^{86}Sr<0.705$, εNd>4; Brophy and Marsh, 1986; Defant and Drummond, 1990; Johnston, 1986). The geochemical characteristics of the CVC, such as high SiO_2

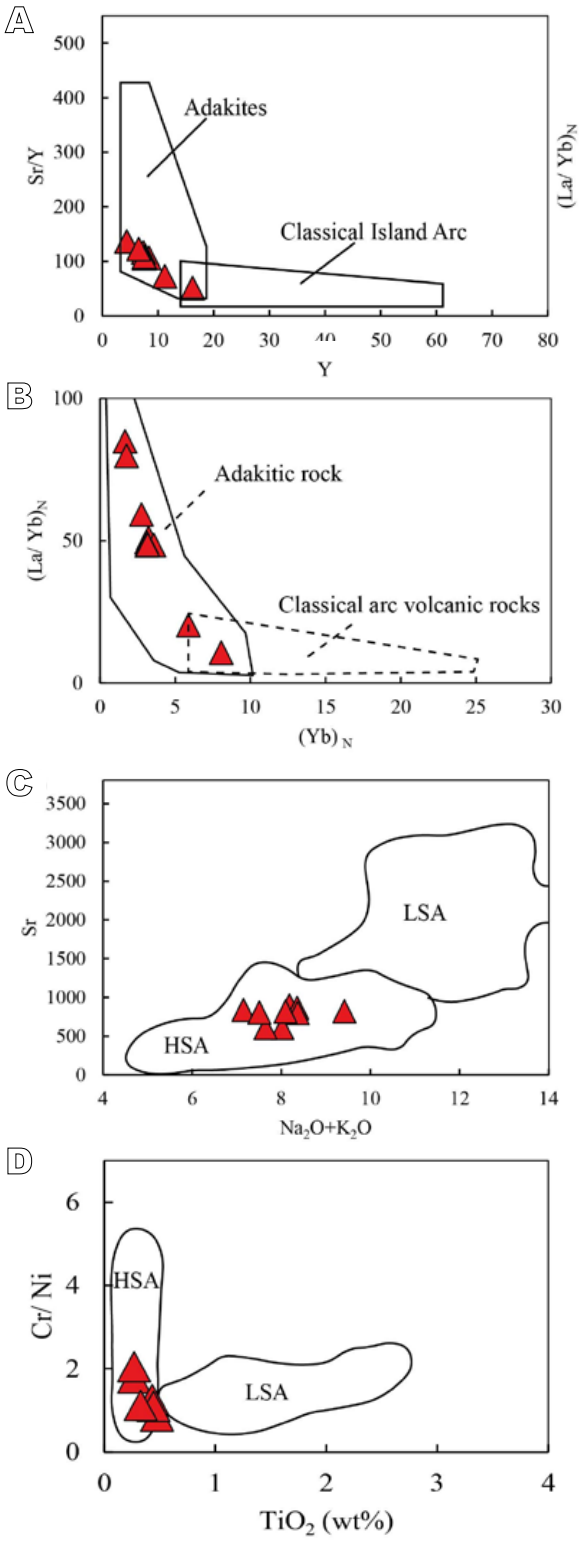

FIGURE 10. A) Sr/Y versus Y (Defant and Drummond, 1990). B) (La/Yb)N versus (Yb)N (Reich *et al.*, 2003), showing the adakitic affinity of the Chenar Volcanic Cone. C) Sr versus Na_2O+K_2O (wt%). D) Cr/Ni versus TiO_2 (wt%). Compositions of High-Silica Adakites (HAS) and Low-Silica Adakites (LSA) are from Martin *et al.* (2005).

(av. 67.53wt%), low MgO (av. 0.92wt%) and compatible element (Cr<30ppm and Ni< 10ppm) contents are unlike those of mantle origin (Martin *et al.*, 2005).

The diagram K_2O/Na_2O versus Al_2O_3 (after Jamshidi *et al.*, 2018) and ternary diagram of Fe_2O_3-K_2O-MgO for the studied rocks proposed that these adakitic rocks are closely related to interactions between melts of the subducting basaltic oceanic crust and the overlying mantle wedge (Fig. 12A-C).

More, the CVC have generally low MgO, Cr and Ni, a feature shared by adakites in continental collision zones such as Tibet, Dabie and Turkey. In view of the above arguments, a slab melt origin for the CVC appears very unlikely.

Also, oceanic subduction-related adakitic magmas generally have higher contents of siderophile elements, such as Ni= 1860ppm, Co= 102ppm, Cr= 2520ppm (O'Neill and Palme, 1998), which are not observed in the CVC. Furthermore, it is unlikely that magma mixing between mafic and felsic magmas were involved in their genesis. Magma mixing generally requires mantle-derived

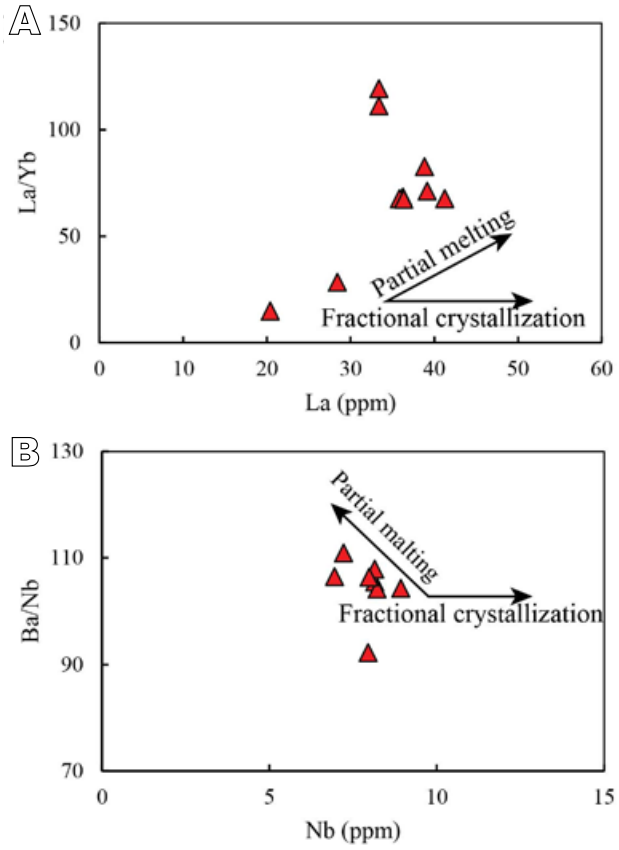

FIGURE 11. A) La/Yb vs. La and B) Ba/Nb vs. Nb (Bourdon *et al.*, 2002) diagrams, revealing a partial melting trend for the Chenar Volcanic Cone (CVC).

basaltic and crust-derived felsic end members (*e.g.* Streck *et al.*, 2007). These resulting adakitic rocks often have relatively high MgO (>0.45%) contents and Mg# (>66) values. Finally, all volcanic rocks in Chenar area have low MgO (0.45wt.%) and Mg# (19.74-37.84) contents, which contradict the two distinct end-members mixing model. The high Al (84988-95121ppm), Sr (605-899ppm) and Sr/Y (106-136) and low Y (4.43-16.23), K_2O (2.4–3.6wt.%), Cr (2.5–10.0ppm) and Ni (1.4–8.5ppm), and high Th (5.6–13.2ppm) contents for the Chenar HAS rocks imply that they were formed by partial melting from melting of modified mantle under the influence of metasomatized subducted oceanic slab. Primary melts formed from partial melting of asthenosphere mantle have Mg# >0.70, whereas differentiated melts have much lower Mg# (<0.60). The reduction of Mg# in the melt is the result of the primary crystallization of olivine MgO decreases compared to FeO (Grove *et al.*, 2003, 2012).

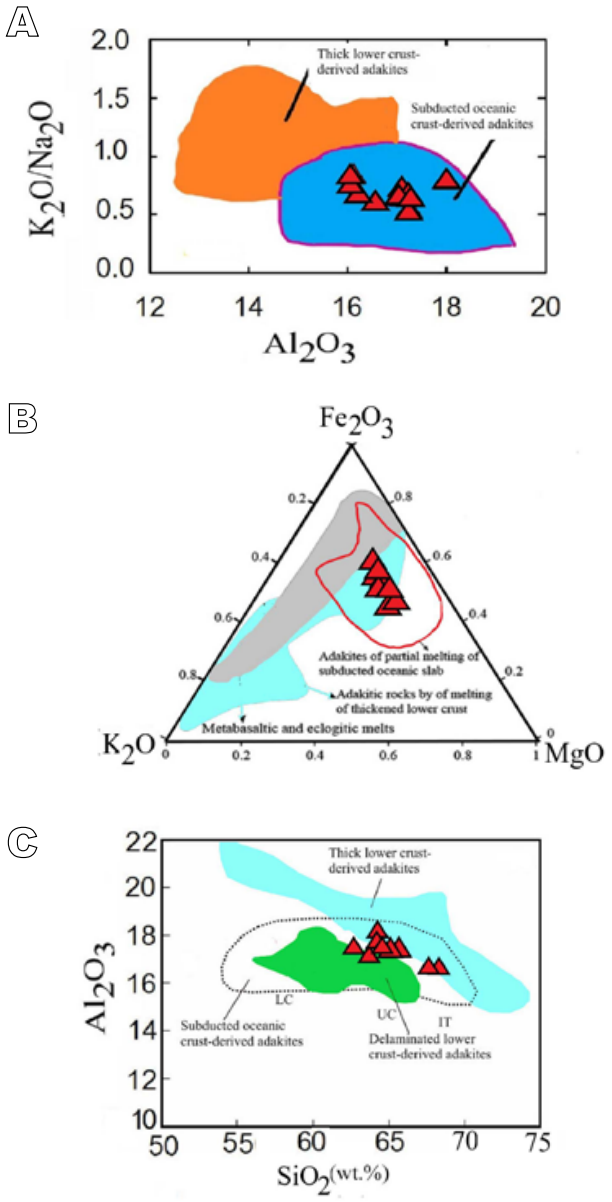

FIGURE 12. A) (K_2O/Na_2O) versus Al_2O_3 diagram (after Jamshidi *et al.*, 2018). B) Ternary diagram of Fe_2O_3-K_2O-MgO for the studied granitoids. Data for adakites originated by partial melting of the subducted oceanic crust are from: Aguillón-Robles *et al.*, 2001; Defant and Drummond, 1993; Kay *et al.*, 1993; Stern and Kilian, 1996; Yogodzinski *et al.*, 1995. Data for adakitic rocks derived by partial melting of thickened lower crust are from: Wang *et al.*, 2004; Wang *et al.*, 2006; Xu *et al.*, 2007. Data for thick lower-crust-derived adakites are from: Atherton and Petford, 1993; Johnson *et al.*, 1997; Muir *et al.*, 1995; Petford and Atherton, 1996. C) Al_2O_3 versus SiO_2 diagram (Wang *et al.*, 2008).

Enrichment of LILEs and LREEs over the HFSEs, negative Nb-Ta and Ti anomalies in the primitive mantle-normalized spider diagrams (Fig. 8A-B) are more consistent with involvement of lower crust. Adakites generated by partial melting of delaminated lower crust contain high Cr and Ni contents (Gao *et al.*, 2004). Different magma sources can also be effectively constrained using a multi-element diagram of Sr/Y versus $(La/Yb)_N$ (Ling *et al.*, 2011; Liu *et al.*, 2010; Sun *et al.*, 2011). Also, the CVC plotted in the range of subducted oceanic crust-derived adakites (Fig. 13A-C). Based on Yumul *et al.* (2017), the mechanism of formation for adakitic rocks has been extended to contain lower crust melting, slab melt-mantle interaction, high pressure fractionation, possibly with sediment melting (subduction erosion) and ridge subduction, among others. These mantle-related magmas are characterized by significantly increased MgO (>3 wt%), Cr and Ni concentrations, and high Mg# values (>50) (Xu *et al.*, 2008), originating from a lithospheric mantle previously depleted by fluids/ Subduction zone melts have been metasomatized.

Garnet is the only rock-forming mineral that can substantially enhance $(La/Yb)_N$ and $(Dy/Yb)_N$ ratios of magma. So, the positively correlated $(La/Yb)_N$ and $(Dy/Yb)_N$ ratios (Fig. 13D) indicate the important role of garnet in their petrogenesis. Additionally, the Hf/Sm vs. Ta/La based plot indicates metasomatism by subduction fluids (LaFlèche *et al.*, 1998) and mantle origin of the adakitic rocks of the region (Fig. 14A).

The CVC from the southeastern UDMA have radiogenic εHf(t) values (+3.1 to +12.7, Fig. 6) that supported a significant involvement of mantle in their origin and homogeneous isotopic compositions. Adakite rocks in Central Iran have two sources: i) melting of a part of the thick lower crust and ii) melting of the subducted Neotethys oceanic slab (Ghadami *et al.*, 2008).

Similarly, lower crust-derived adakites have greater Rb and K_2O/Na_2O ratios than adakites from subducted plates (Delavari *et al.*, 2014). Th, Rb and K_2O/Na_2O in subducted

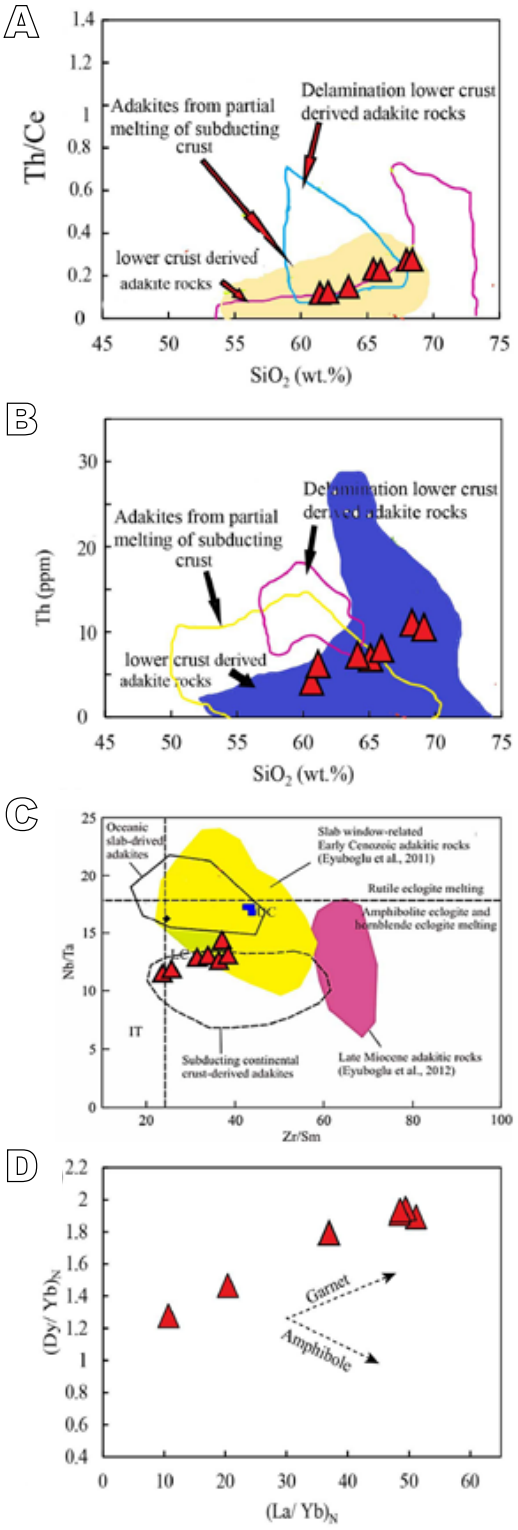

FIGURE 13. A, B) Wang *et al.*, 2006. C) Nb/Ta versus Zr/Sm diagram (Eyuboglu *et al.*, 2012). D) $(La/Yb)_N$ versus $(Dy/Yb)_N$ diagrams for the Chenar Volcanic Cone (CVC). Crystal fractionation trend line for garnet and amphibole are after He *et al.* (2011). Subducting oceanic crust-derived adakites (Wang *et al.*, 2006), delaminated lower crust-derived adakites (Wang *et al.*, 2004, 2006; Xu *et al.*, 2007), thick lower crust-derived adakites (Atherton and Petford, 1993; Johnson *et al.*, 1997; Muir *et al.*, 1995; Petford and Atherton, 1996).

plate adakites are 4.5ppm, 41ppm and 0.35, respectively, while in the study area they are 13.48ppm, 61.71ppm and 0.70 for the adakite originating from melting the lower crust (Drummond *et al.*, 1996). Assuming the lower crust origin for adakite genesis, some researchers have considered the existence of a crust thicker than 50km as a necessary precondition (Hou *et al.*, 2007; Topuz *et al.*, 2005; Wang *et al.*, 2005; Wang *et al.*, 2006). However, experimental studies have shown that partial melting of the lower mafic crust at a depth of 30 to 40km and a temperature of 800 to 900ºC can produce adakit melts, and the lower crust is not needed to undergo the conditions of the eclogite facies (Qian and Hermann, 2013). According to the Moho depth map of the shell, the thickness of the region varies from 48 to 50km (Dehghani and Makris, 1984).

Additionally, adakites due to melting of subducted oceanic crust have Mg# 58-72 and low Rb/Sr ratio of 0.01-0.04ppm (Drummond *et al.*, 1996; Rapp and Watson, 1995), whereas adakites generated by the melting of thickened lower continental crust have Rb/Sr ratio >0.05ppm and Mg# 21-54 (Drummond *et al.*, 1996; Hou *et al.*, 2004). Thus, the Rb/Sr ratio of 0.07-0.14ppm and Mg# 21.15-35.82 in the CVC refers to their formation from the basaltic composition that results from the partial melting of the lithospheric mantle caused by the rise of the hot asthenospheric mantle. (Davies and Blackenburg, 1995; Haschke and Ben-Avraham, 2005). Al_2O_3-K_2O/Na_2O diagram shows that the adakites of the region have a high content of Al_2O_3 and a low K_2O/Na_2O ratio, which indicates the melting process of part of the lithospheric mantle(Yang *et al.*, 2022) (Fig. 12C-D).

TECTONIC IMPLICATIONS

The most important geochemical characteristics of the CVC are its adakitic signatures (HSA), such as their high Sr/Y (~51.6-136.8) at low Y (~4.43–16.2ppm) and high La/Yb (~28.4-118.4) at low Yb (~0.2-1.3ppm) (Fig. 10A-B). Many researchers have suggested that adakites in Iran were produced by melting of the oceanic slab beneath the Iranian microcontinent (*e.g.* Omrani *et al.*, 2008) or by the partial melting of the plum mantle during or after the collision of the Iranian-Arabian plates (Jamali and Mehrabi, 2015). Additionally, these rocks plot in the field of post-collisional adakite on the Th/Yb versus Th/Sm and Th versus Th/Ce diagrams (Fig. 14B-C), as is expected for UDMA continental arc volcanism.

Aftabi and Atapour (2021) stated that petrogeochemical and metallogenic evolution of the Kerman Cenozoic arc involved five magmatic phases: The third phase of magmatism is the formation of dacite domes during the Middle-Upper Miocene, in which adakitic volcano related

to subduction is formed in a flat continental arc. Many geological and geophysical observations, as well as models for magmatism for the Iranian and East Anatolian plateaus can be reconciled in a context of break-off of the Neo-Tethys oceanic slab or the delamination of mafic lithosphere

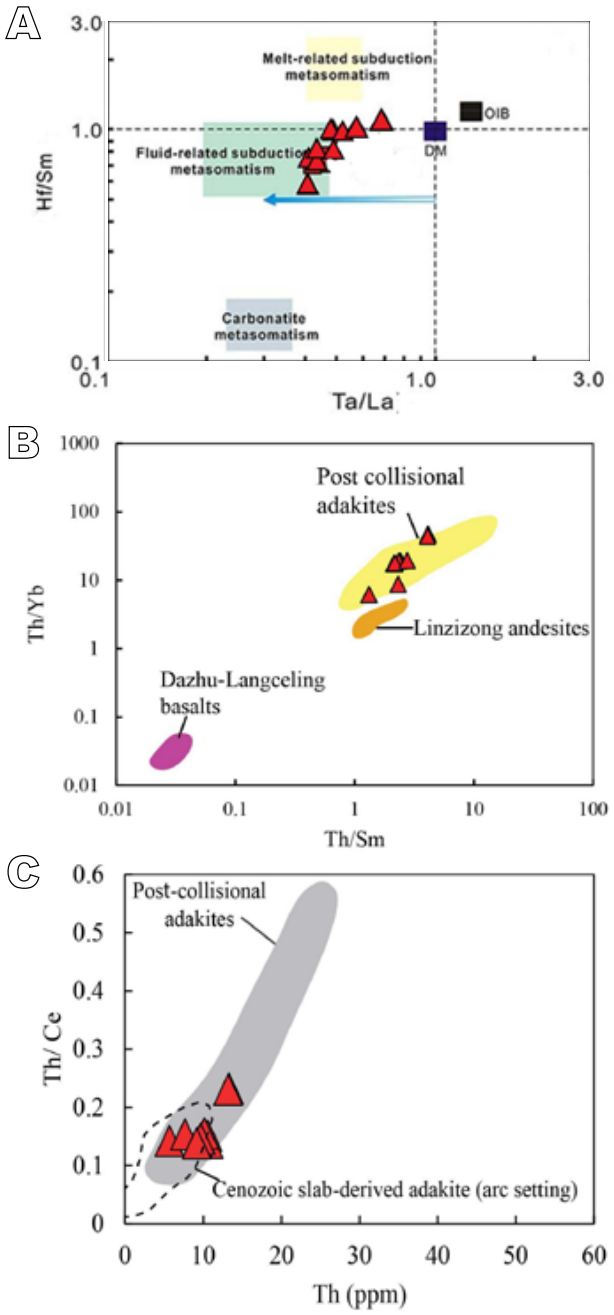

FIGURE 14. A) (Hf/Sm) versus (Ta/La) diagram to determine the origin of the Chenar Volcanic cone (LaFlèche *et al.*, 1998). B) Th/Yb versus Th/Sm diagram (Zhu *et al.*, 2009) and C) Th/Ce versus Th (Wang *et al.*, 2008) diagram for discriminating the tectonic setting of the Chenar Volcanic Cone. Fields of post-collisional adakites (Chung *et al.*, 2003), Linzizong andesites (Mo *et al.*, 2007) and Cenozoic slab-derived adakites (arc setting; Hou *et al.*, 2004; Guo *et al.*, 2007; Wang *et al.*, 2008).

beneath the Bitlis-Zagros suture region (*e.g.* Agard *et al.*, 2011; Hatzfeld and Molnar, 2010; Keskin, 2003; Molinaro *et al.*, 2005; Omrani *et al.*, 2008; Şengör *et al.*, 2003). This is supported by the development of transpressive zones with oblique compressive tectonism (Haschke and Gunther, 2003; Kheirkhah *et al.*, 2020; Sillitoe, 1998; Verdel *et al.*, 2011; Zhang *et al.*, 2017), transpressive shortening of the Iranian microplate up to crustal thickness of 40–50km (Dehghani and Makris, 1983; Rapp *et al.*, 1999), and subduction of the Neotethyan oceanic slab under a rotating Iranian microcontinent, possible shift in the arc axis towards the east and shifting axis of magmatism toward the central-southeast of the Urumieh-Dokhtar magmatic belt (Babazadeh *et al.*, 2018; Dercourt *et al.*, 1986).

Zircon Hf isotope data show that Himalayan-Tibet syn-collisional (<55Ma) igneous rocks have more heterogeneous εHf(t) than pre-collisional subduction-related rocks, likely reflecting increased assimilation of thickened crust (Alexander *et al.*, 2019).

Neotethys-related late Cretaceous to Pleistocene subduction- and collision-related magmatic rocks from the ~350km long southeastern UDMA of Iran provide an excellent natural laboratory to better understand these processes. Significant changes in magmatic compositions reflect initial collision with Arabia at ~32Ma, changing from normal calc-alkaline to increasingly adakitic immediately after collision began. Shafaii Moghadam *et al.* (2022) identified five stages: i) normal continental-arc magmatism during the late Cretaceous; ii) arc quiescence in Paleocene and early Eocene time; iii) middle-late Eocene extensional arc magmatism related to slab rollback; iv) early collision and crustal thickening during the early Oligocene and v) slab breakoff, asthenospheric upwelling and associated adakitic magmatism from middle Miocene onward. Temporal changes in UDMA magmas reflect the response of the overriding plate to changes in the geometry of the subducting Neotethyan lithosphere and to collision between Arabia and Iran. Crustal thickening and arc narrowing during Miocene to Pleistocene post-collisional magmatism caused adakitic magmatism (Shafaii Moghadam *et al.*, 2022). Figure 15 shows 5 different models for the formation of adakites from the crust and mantle (Zhang *et al.*, 2019).

CONCLUSIONS

Zircon U-Pb geochronology of the dacitic to rhyodacitic CVC rocks of the southeastern part of the UDMA supports a late Miocene age. Whole-rock geochemical analysis shows a high-silica adakitic affinity, and calc-alkaline to shoshonitic nature, *i.e.* an arc-like source. The geochemical features characterized by enrichment of LILEs and LREEs relative to HFSE and HREE and Y, and negative Nb, Ti anomalies,

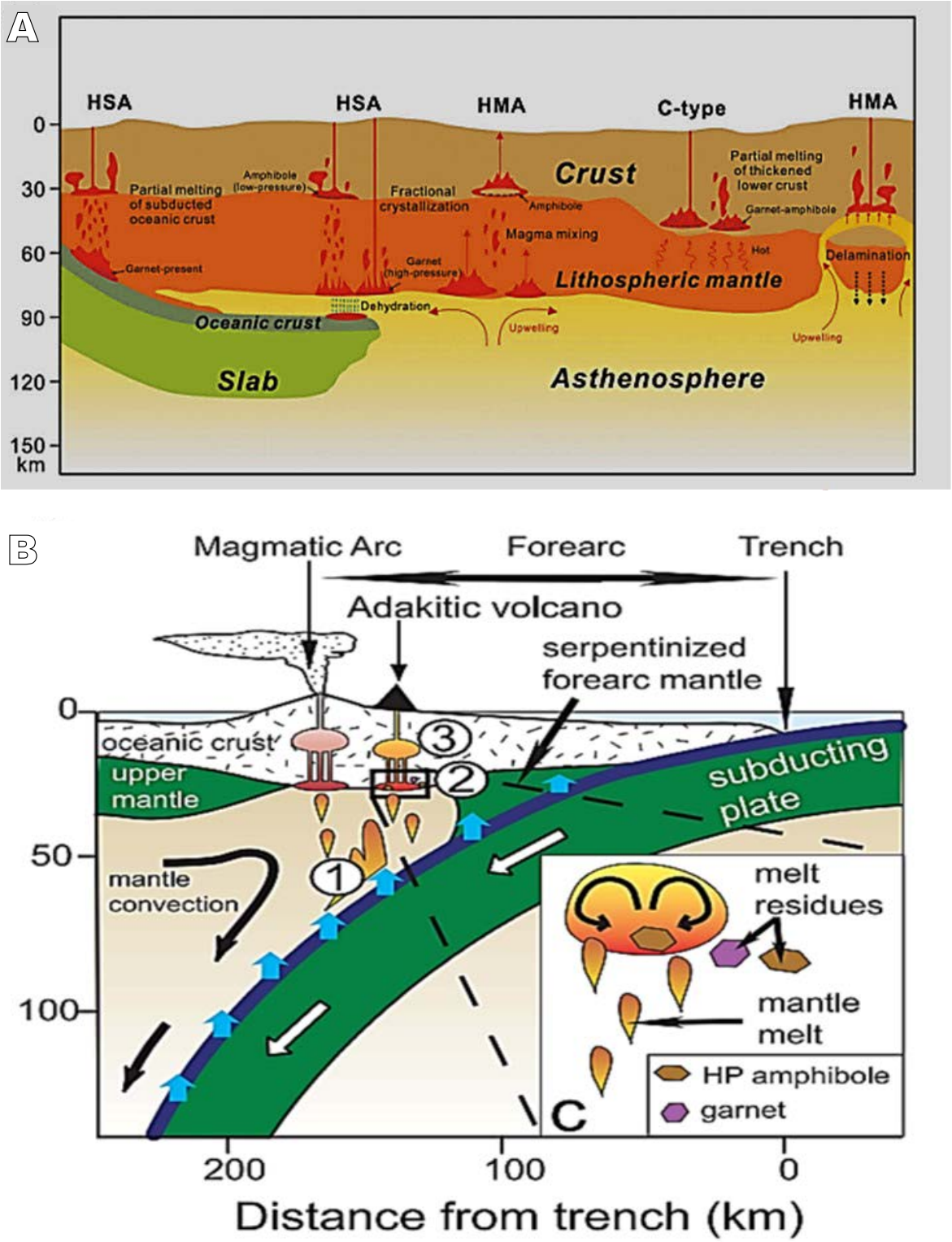

FIGURE 15. A) Five genetic models for the formation of adakites or adakitic rocks. As discussed in this article, adakitic are formed in different geological environments. HSA: High SiO_2 Adakites, HMA: High Mg# Adakites, C-type: type C Adakite rocks (Zhang *et al.*, 2019b). B) Petrogenesis of adakite from fractionated mantle melts. i) Basaltic arc melts (in orange) form by hydrous melting of the sub-arc mantle wedge and stall in ii) lower (30km depth) and iii) upper crustal magma storage regions. Slab melts may flux the sub-arc mantle wedge and mix or mingle with the mantle melts at lower crustal depths. C) Close-up of the lower crustal magma reservoir, where mantle melts fractionate garnet and form adakitic melts (*e.g.* Rooney *et al.*, 2011; Kimura *et al.*, 2014).

indicate a source that was geochemically and enriched by subduction zone processes, *i.e.* having an arc association. The geochemical characteristics of the studied rocks, such as their high Sr/Y (~51.6–136.8) at low Y (~4.4–16.2ppm) and high La/Yb (~28.4–118.4) at low Yb (~0.2–0.3ppm), are indicative of high-silica HSA. Chondrite-normalized plot of REE shows steeply increasing slope from LREE to HREE and a positive Ce anomaly (Ce/Ce^*= 1.6-36.6) that probably indicate relatively oxidizing conditions for the CVC parental magma. Zircon Hf isotope data show that the samples from the CVC are in the range of continental crust, indicating their origin. The whole-rock positive Eu/Eu^* anomaly and zircon Ce/Ce^* anomaly confirm that a basaltic lower-crustal source would have been arc-generated originally. According to the geochemical features of the Dehaj-Sarduiyeh volcano-sedimentary belt, these rocks were derived from partial melting of asthenospheric mantle. Tectonic discrimination diagrams clearly illustrate CVC belonging to the post-collisional environment, which is in agreement with the tectono-magmatic environment proposed for the UDMA.

DECLARATION OF COMPETING INTEREST

The authors declare that they have no known competing financial interests or personal relationships that could have appeared to influence the work reported in this paper.

ACKNOWLEDGMENTS

Partial support from Shahid Bahonar Kerman University (Iran) is acknowledged. The manuscript benefitted from several detailed reviews and comments from the Associate Editor that helped a lot with the clarity of presentation.

REFERENCES

Atapour, H., 2009. Comments on "Arc-magmatism and subduction history beneath the Zagros Mountains, Iran: A new report of adakites and geodynamic consequences" by J. Omrani, P. Agard, H. Whitechurch, M. Benoit, G. Prouteau, L. Jolivet. Lithos, 113, 844-846.

Agard, P., Omrani, J., Jolivet, L., Whitechurch, H., Vrielynck, B., Spakman, W., Monié, P., Meyer, B., Wortel, R., 2011. Zagros orogeny: a subduction-dominated process. Geological Magazine, 148(5-6), 692-725.

Amelin, Y., Lee, D.C., Halliday, A.N., 2000. Early-middle Archaean crustal evolution deduced from Lu-Hf and U-Pb isotopic studies of single zircon grains. Geochim Cosmochim Acta, 64, 4205-4225. DOI: https://doi.org/10.1016/S0016-7037(00)00493-2

Aguillón-Robles, A., Calmus, T., Benoit, M., Bellon, H., Maury, R.C., Cotton, J., Bourgois, J., Michaud, F., 2001. Late Miocene adakites and Nb-enriched basalts from Vizcaino Peninsula, Mexico: Indicators of East Pacific Rise subduction below southern Baja California. Geology, 29(6), 531-534.

Ahmadian, J., Sarjoughian, F., Lentz, D., Esna-Ashari, A., Murata, M., Ozawa, H., 2016. Eocene K-rich adakitic rocks in the Central Iran: implications for evaluating its Cu–Au–Mo metallogenic potential. Ore Geology Reviews, 72, 323-42.

Alexander, E., Wielicki, M., Harrison, T., DePaolo, D., Zhao, Z., Zhu, D., 2019. Hf and Nd isotopic constraints on pre-and syn-collisional crustal thickness of southern Tibet. Journal of Geophysical Research, Solid Earth, 124 (11), 11038-11054.

Arvin, M., Pan, Y., Dargahi, S., Malekizadeh, A., Babaei, A., 2007. Petrochemistry of the Siah Kuh granitoid stock southwest of Kerman, Iran: Implications for initiation of Neotethys subduction. Journal Asian Earth Science, 30, 474-489.

Asadi, A., Moore, F., Zarasvandi, A., 2014. Discriminating productive and barren porphyry copper deposits in the southeastern part of the central Iranian volcano – plutonic belt, Kerman region, Iran: A review. Earth-Science Reviews, 138, 25-46.

Atapour, H., Aftabi, A., 2021. Petrogeochemical evolution of calcalkaline, shoshonitic and adakitic magmatism associated with Kerman Cenozoic arc porphyry copper mineralization, southeastern Iran: A review. Lithos, 398-399. DOI: doi.org/10.1016/j.lithos.2021.106261

Atherton, M.P., Petford, N., 1993. Generation of sodium-rich magmas from newly underplated basaltic crust. Nature, 362, 144-146.

Azizi, H., Stern, R.J., 2019. Jurassic igneous rocks of the Central Sanandaj-Sirjan zone (Iran) mark a propagating continental rift, not a magmatic arc. Terra Nova, 31, 415-423.

Azizi, H., Asahara, Y., Tsuboi, M., Takemura, K., Razyani, S., 2014. The role of the heterogenetic mantle in the genesis of adakites northeast of Sanandaj, northwestern Iran. Geochemistry, 74, 87-97.

Babazadeh, S., Ghorbani, M.R., Cotte, J.M., Borcker, M., 2018. Multistage tectonomagmatic evolution of the central Urmieh-Dokhtar magmatic arc, south Ardestan, Iran: insights from zircon geochronology and geochemistry. Geology, 33, 1-6.

Belousova, E.A., Griffin, W.L., Suzanne, Y.O.R., Fisher, N.I., 2002. Igneous zircon: trace element composition as an indicator of source rock type. Contributions to Mineralogy and Petrology, 143, 602-622.

Belousova, E.A., Kostitsyn, Y.A., Griffin, W.L., Begg, G.C., O'Reilly, S.Y., Pearson, N.J., 2010, The growth of the continental crust: Constraints from zircon Hf-isotope data. Lithos, 119, 457-466. DOI: 10.1016/j.lithos.2010.07.024

Berberian, F., Berberian, M., 1981 Tectono-plutonic episodes in Iran. In: Gupta, H.K., Delany, F.M. (eds.). Zagros, Hindukosh, Himalaya. Washington DC, Geodynamic Evolution American Geophysical union, 5-32.

Berberian, M., King, G.C., 1981. Towards a paleogeography and tectonic evolution of Iran. Canadian Journal of Earth Sciences 18, 210-265.

Bourdon, E., Eissem, J.P., Monzier, M., Robin, C., Martin, H., Cotton, J., Hall, M.L., 2002. Adakite-like lavas from Antisana Volcano (Ecuador): evidence for slab melt metasomatism beneath the Andean northern volcanic zone. Journal of Petrology, 43, 199-217.

Bouvier, A., Vervoort, J.D., Patchett, P.J., 2008. The Lu–Hf and Sm–Nd isotopic composition of CHUR: constraints from unequilibrated chondrites and implications for the bulk composition of terrestrial planets. Earth and Planetary Science Letters, 273, 48-57.

Brophy, J.G., Marsh, B.D., 1986. On the origin of high-alumina arc basalt and the mechanics of melt extraction. Journal of Petrology, 27(4), 763-789. DOI: 10.1093/petrology/27.4.763

Castillo, P.R., 2006. An overview of adakite petrogenesis. Chinese Science Bulletin, 51, 258-268.

Castillo, P.R., 2012. Adakite petrogenesis. Lithos, 134, 304-316.

Castillo, P.R., Janney, P.E., Solidum, R.U., 1999. Petrology and geochemistry of Camiguin Island: southern Philippines: insights to the source of adakites and other lavas in a complex arc setting. Contributions to Mineralogy and Petrology, 134, 33-51.

Chiaradia, M., Muntener, O., Beate, B., Fontignie, D., 2009. Adakite–like volcanism of Ecuador: lower crust magmatic evolution and recycling. Contributions to Mineralogy and Petrology, 158, 563-588.

Chung, S.L., Liu, D.Y., Ji, J.Q., Chu, M.F., Lee, H.Y., Wen, D.J., Lo, C.H., Lee, T.Y., Qian, Q., Zhang, Q., 2003. Adakites from continental collision zones: Melting the of thickened lower crust beneath southern Tibet. Geology, 31, 1021-1024.

Coldwell, B., Clemens, J., Petford, N., 2011. Deep crustal melting in the Peruvian Andes: felsic magma generation during delamination and uplift. Lithos, 125, 272-286.

Corfu, F., Noble, S.R., 1992. Genesis of the southern Abitibi greenstone belt, Superior Province, Canada: Evidence from zircon Hf isotope analyses using a single filament technique. Geochimica Cosmochimica Acta, 56, 2081-2097.

Corfu, F., Stott, G.M., 1998. Shebandowan greenstone belt, western Superior Province: U-Pb ages, tectonic implications, and correlations. Geological Society of America Bulletin, 110, 1467-1484.

Davies, J.H., Blanckenburg, V.F., 1995. Slab break off: a modal of lithosphere detachment and its test in the magmatism and deformation of collisional orogens. Earth and Planetary Science Letters, 129, 85-102.

Defant, M.J., Drummond, M.S., 1990. Derivation of some modern arc magmas by melting of the young subducted lithosphere. Nature, 347, 662-665.

Defant, M.J., Drummond, M.S., 1993. Mount St. Helens: Potential example of the partial melting of the subducted lithosphere in a volcanic arc. Geology, 21(6), 547-550.

Defant, M.J., Kepezhinskas, P., Defant, M.J., Xu, J.F., Kepezhinskas, P., Wang, Q., Zhang, Q., Xiao, L., 2002. Adakites: some variations on a theme. Acta Petrologica Sinica, 18, 129-142.

Dehghani, G.A., Makris, T., 1983. The gravity field and crustal structure of Iran. Geological Survey of Iran Report, 51, 51-68.

Dehghani, G.A., Makris, T., 1984. The gravity field and crustal structure of Iran. Neues Jahrbuch fur Geologie und Palaontologie-Abhandlun-gen, 168(2-3), 215-229.

Delavari, M., Amini, S., Schmitt, A.K., McKeegan, K.D., Harrison, T.M., 2014. U–Pb geochronology and geochemistry of Bibi-Maryam pluton, eastern Iran: implication for the late stage of the tectonic evolution of the Sistan Ocean. Lithos, 200, 197-211.

Dercourt, J., Zonenshain, L., Ricou, L.E., Kazemian, V.G., 1986. Geologic evolution of the Tethys belt from the Atlantic to Pamirs since the Lias. Tectonophysics, 123, 241-315.

Dhuime, B., Hawkesworth, C., Cawood, P., Storey, C., 2012. A change in the geodynamics of continental growth 3 billion years ago. Science, 335, 1334-1336.

Dimitrijevic, M.D., 1973. Geology of the Kerman region. Geological Survey of Iran Report, 52, 334pp.

Drummond, M.S., Defant, M.J., Kepezhinskas, P.K., 1996. Petrogenesis of slab derived trondhjemite-tonalite-dacite/adakite magmas. Transactions of the Royal Society of Edinburgh. Earth Sciences, 87(1-2), 205-215.

Eyuboglu, Y., Santosh, M., Yi, K., Bektas, O., Kwon, S., 2012. Discovery of Miocene adakitic dacite from the Eastern Pontides belt and revised geodynamic model for the late Cenozoic evolution of the eastern Mediterranean region. Lithos, 146-147, 218-232.

Fang, H., Sheng, H.F., 2010. Partial melting of the dry mafic continental crust: Implications for petrogenesis of C-type adakites. Geochemistry, 55, 1-12.

Gao, S., Rudnick, R.L., Yuan, H.L., Liu, X.M., Liu, Y.S., Xu, W.L., Ling, W.L., Ayers, J., Wang, X.C., Wang, Q.H., 2004. Recycling lower continental crust in the North China craton. Nature, 432, 892-897.

Gao, Y.F., Yang, Z.S., Hou, Z.Q., Wei, R.H., Meng, X.J., Tian, S.H., 2010. Eocene potassic and ultrapotassic volcanism in south Tibet: new constraints on mantle source characteristics and geodynamic processes. Lithos, 117, 20-32.

Ghadami, G.R., Nazarinia, A., 2021. Adakite signature of granitoids in the northwest of Shahr-e- Babak, Kerman, Iran: constrains on geochemistry. Journal of Mineralogy and Geochemistry, 197(3), 263-283.

Ghadami, G., Shahre Babaki, A.M., Mortazavi, M., 2008. Post-Collisional Plio-Pleistocene Adakitic Volcanism in Centeral Iranian Volcanic Belt: Geochemical and Geodynamic Implications. Islamic Republic of Iran. Journal of Sciences, 19(3), 223-235.

Green, N.L., Harry, D.L., 1999. On the relationship between subducted slab age and arc basalt petrogenesis, Cascadia subduction system, North America. Earth and Planetary Science Letters, 171, 367-381.

Griffin, W.L., Pearson, N.J., Belousova, E., Jackson, S.E., Van Achterbergh, E., O'Reilly, S.Y., Shee, S.R., 2000. The Hf isotope composition of cratonic mantle: LAM-MC-ICPMS analysis of zircon megacrysts in kimberlites. Geochimica et Cosmochimica Acta, 64, 133-147. DOI: doi.org/10.1016/S0016-7037(99)00343-9

Griffin, W.L., Wang, X., Jackson, S.E., Pearson, N.J., O'Reilly, S.Y., Xu, X., Zhou, X., 2002. Zircon chemistry and magma mixing, SE China: in-situ analysis of Hf isotopes, Tonglu and Pingtan igneous complexes. Lithos, 61, 237-269. DOI: doi.org/10.1016/S0024-4937(02)00082-8

Griffin, W.L., Graham, S., O'Reilly, S.Y., Pearson, N.J., 2004. Lithosphere evolution beneath the Kaapvaal Craton: Re–Os systematics of sulfides in mantle-derived peridotites. Chemical Geology, 208, 89-118.

Grove, T.L., Elkins-Tanton, L.T., Parman, S.W., Chatterjee, N., Müntener, O., Gaetani, G.A., 2003. Fractional crystallization and mantle-melting controls on calc-alkaline differentiation trends. Contributions to Mineralogy and Petrology, 145, 515-533.

Grove, T.L., Till, C.B., Krawczynski, M.J., 2012. The role of H_2O in subduction zone magmatism. Annual Review of Earth and Planetary Sciences, 40, 413-439.

Guo, F., Nakamuru, E., Fan, W., Kobayoshi, K., Li, C., 2007. Generation of Paleocene adakitic andesites by magma mixing; Yanji Area, NE China. Journal of Petrology, 48, 661-692.

Guo, J.O., Reilly, S.Y., Griffin, W.L., 1996. Zircon inclusions in corundum megacrysts: I. Trace element geochemistry and clues to the origin of corundum megacrysts in alkali basalts. Geochimica et Cosmochimica Acta, 60, 2347-2363.

Guo, Z.F., Wilson, M., Liu, J.Q., 2007. Post-collisional adakites in south Tibet: products of partial melting of subduction-modified lower crust. Lithos, 96, 205-224.

Harrison, T.M., Blichert-Toft, J., Muller, W., Albarede, F., Holden, P., Mojzsi, S.J., 2005. Heterogeneous Hadean hafnium: evidence of continental crust at 4.4 to 4.5Ga. Science, 310, 1-10.

Haschke, M.R., Gunther, A., 2003. Balancing crustal thickening in arcs by tectonic versus magmatic means. Geology, 31, 933-936.

Hastie, A.R., Kerr, A.C., Pearce, J.A., Mitchell, S., 2007. Classifcation of altered volcanic island arc rocks using immobile trace elements: development of the Th–Co discrimination diagram. Journal of Petrology, 48(12), 2341-2357.

Haschke, M.R., Ben-Avraham, Z., 2005. Adakites from Collision-Modified Lithosphere. Geophysical Research Letters, 32, 14-32. DOI: doi.org/10.1029/2005GL023468

Hatzfeld, D., Molnar, P., 2010. Comparisons of the kinematics and deep structures of the Zagros and Himalaya and of the Iranian and Tibetan plateaus and geodynamic implications. Review of Geophysics, 48, 1-48.

Hawkesworth, C.J., Dhuime, B., Pietranik, A.B., Cawood, P., Kemp, A.I.S., Storey, C.D., 2010. The generation and evolution of the continental crust. Journal of the Geological Society of London, 167, 229-248.

Hoskin, P.W.O., Schaltegger, U., 2003. The composition of zircon and igneous and metamorphic petrogenesis. Reviews in Mineralogy and Geochemistry, 53(1), 27-62.

Hou, Z.Q., Gao, Y.F., Meng, X.L., Qu, X.M., Huang, M., 2004a. Genesis of adakitic porphyry and tectonic controls on the Gangdese Miocene porphyry copper belt in the Tibetan orogen. Acta Petrologica Sinica, 20, 239-248.

Hou, Z.Q., Gao, Y.F., Qu, X.M., Rui, Z.Y., Mo, X.X., 2004b. Origin of adakitic intrusives generated during mid-Miocene east-west extension in southern Tibet. Earth Planetary Science Letter, 220, 39-155.

Hou, M.-L., Jiang, Y.-H., Jiang, S.-Y., Ling, H.-F., Zhao, K.-D., 2007. Contrasting origins of late Mesozoic adakitic granitoids from the northwestern Jiaodong Peninsula, east China: implications for crustal thickening to delamination. Geological Magazine, 144(4), 619-631.

Iizuka, T., Komiya, T., Rino, S., Maruyama, S., Hirata, T., 2010. Detrital zircon evidence for Hf isotopic evolution of granitoid crust and continental growth. Geochimica et Cosmochimica Acta, 74, 2450-2472.

Imer, A., Richards, J.P., Creaser, R.A., 2014. The late Oligocene Cevizlidere Cu-Au-Mo deposit, Tunceli Province, eastern Turkey Mineral Deposita, 50, 245–263. DOI: doi.org/10.1007/s00126-014-0533-4/

Jackson, S.E., Pearson, N.J., Griffin, W.L., Belousova, E.A., 2004. The Application of Laser Ablation-Inductively Coupled Plasma-Mass Spectrometry to In Situ U-Pb Zircon Geochronology. Chemical Geology. 211, 47-69. DOI: 10.1016/j.chemgeo.2004.06.017

Jamali, H., Mehrabi, B., 2015. Relationships between arc maturity and Cu–Mo–Au porphyry and related epithermal mineralization at the Cenozoic Arasbaran magmatic belt. Ore Geology Reviews, 65, 481-501.

Jamshidi, D., Ghasemi, H., Miao, L.C., Sadeghian, M., 2018. Adakite magmatism within the Sabzevar ophiolite zone, NE Iran: U-Pb geochronology and Sr-Nd isotopic evidences. Geopersia, 8, 11-30.

Jiang, J.H., Wang, R.J., Qu, X.M., Xin, H.B, Wang, Z.Z., 2011. Crustal extension of the Bangong Lake Arc Zone, Western Tibetan Plateau, after the closure of the Tethys Oceanic Basin (in Chinese with English abstract). Earth Science, 36(6), 1021-1032.

Jiang, Y.H., Jiang, SH., Zhao, K.D., Feiling, H., 2006. Petrogenesis of Late Jurassic Qianlishan granites and mafic dykes, Southeast China: implications for a back-arc extension setting. Geological Magazine, 143(4), 457-474.

Johnston, A.D., 1986. Anhydrous P-T phase relations of near-primary high-alumina basalt from the South Sandwich Islands: implications for the origin of island arcs and tonalite-trondhjemite. Contributions to Mineralogy and Petrology, 92, 368-382.

Johnson, K., Barnes, C.G., Miller, C.A., 1997. Petrology, geochemistry and genesis of high- Al tonalite and trondhjemites of the Cornucopie stock, Blue Mountains, northwestern Orogen. Journal of Petrology, 38, 1585-1611.

Karsli, O., Dokuz, A., Kandemir, R., Aydin, F., Schmitt, A.K., Ersoy, E.Y., Alyıldız, C., 2019. Adakite-like parental melt generation by partial fusion of juvenile lower crust, Sakarya Zone, NE Turkey: a far-field response to break-off of the southern Neotethyan oceanic lithosphere. Lithos, 338, 58-72.

Kay, R.W., 1987. Aleutian magnesian andesite: melts from subducted Pacific Ocean crust. Journal of Volcanology and Geothermal Research, 4, 117-132.

Kay, R.W., Kay, S.M., 2002. Andean adakites three ways to make them. Acta Petrologica Sinica, 18, 303-311.

Kemp, A.I.S., Hawkesworth, C.J., Paterson, B.A., Kinny, P., 2006. Episodic growth of the Gondwana Supercontinent from hafnium and oxygen isotopes in zircon. Nature, 439, 580-588.

Keskin, M., 2003. Magma generation by slab steepening and breakoff beneath a subduction accretion complex: an alternative model for collision-related volcanism in Eastern Anatolia, Turkey. Geophysical Research Letter, 30, 46-80.

Kheirkhah, M., Neill, I., Allen, M.B., Emami, M.H., Shahraki Ghadimi, A., 2020. Distinct sources for high-K and adakitic magmatism in SE Iran. Journal of Asian Earth Sciences, 196, 104-355.

Kirkland, C.L., Smithies, R.H., Spaggiari, C.V., 2015, Foreign contemporaries—Unravelling disparate isotopic signatures from Mesoprotero-zoic Central and Western Australia. Precambrian Research, 265, 218-231. DOI: doi.org/10.1016/j.precamres.2014.12.001

Kogiso, T., Tatsumi, Y., Nakano, S., 1997. Trace element transport during dehydration processes in the subducted oceanic crust: 1. Experiments and implications for the origin of ocean island basalts. Earth and Planetary Science Letters, 148, 193-205.

LaFlèche, M.R., Camire, G., Jenner, G.A., 1998. Geochemistry of post-Acadian, Carboniferous continental intraplate basalts from the Maritimes Basin, Magdalen islands, Quebec, Canada. Chemical Geology, 148, 115-136.

Ling, M.X., Wang, F.Y., Ding, X., Zhou, J.B., Sun, W.D., 2011. Different origins of adakites from the Dabie Mountains and the Lower Yangtze River Belt, eastern China: geochemical constraints. International Geology Review, 53, 727-740.

Liu, S.A., Li, S., He, Y., Huang, F., 2010. Geochemical contrasts between early Cretaceous ore-bearing and ore-barren high-Mg adakites in central-eastern China: implications for petrogenesis and Cu–Au mineralization. Geochimica et Cosmochimica Acta, 74, 7160-7178.

Macpherson, C.G., Dreher, S.T., Thirlwall, M.F., 2006. Adakites without slab melting: high pressure differentiation of island arc magma, Mindanao, the Philippines. Earth and Planetary Science Letter, 243, 581-593.

Martin, H., Smithies, R.H., Rapp, R., Moyen, J.F., Champion, D., 2005. An overview of adakite, tonalite–trondhjemite–granodiorite (TTG), and sanukitoid: relationships and some implications for crustal evolution. Lithos, 79, 1-24.

Mazhari, S.A., 2016. Petrogenesis of adakite and high-Nb basalt association in the SW of Sabzevar Zone, NE of Iran: evidence for slab melt-mantle interaction. Journal of African Earth Science, 116, 170-181.

McDonough, W.F., Sun, S.S., 1995. The composition of the Earth. Chemical Geology, 120, 223-253.

Mo, X.X., Hou, Z.Q., Niu, Y.L., Dong, G.C., Qu, X.M., Zhao, Z.D., Yang, Z.M., 2007. Mantle to crustal thickening during continental collision: evidence from Cenozoic igneous rocks in southern Tibet. Lithos, 96, 225-242.

Moghadam, H.S., Li, Q.L., Griffin, W.L., Stern, R.J., Santos, J.F., Ducea, M.N., Ottley, Ch.J, Karsli, O., Sepidbar, F., O'Reilly, S.Y., 2022. Temporal changes in subduction-to collision-related magmatism in the Neotethyan orogen: The Southeast Iran example. Earth-Science Reviews, 226, 93-103.

Molinaro, M., Zeyen, H., Laurencin, X., 2005. Lithospheric structure beneath the southeastern Zagros Mountains, Iran: recent slab break-off? Terra Nova, 17, 1-6.

Moradian, A., 1997. Geochemistry, geochronology and petrography of feldspathoid-bearing rocks in the Urumieh-Dokhtar volcanic belt, Iran. PhD Thesis. New South Wales (Australia), University of Wollongong, i-xvii, 412pp.

Moyen, J.F., 2009. High Sr/Y and La/Yb ratios: the meaning of the adakitic signature. Lithos, 112, 556-547.

Muir, R.J., Weaver, S.D., Bradshaw, J.D., Eby, G.N., Evans, J.A., 1995a. Geochemistry of the Cretaceous separation Point batholith, New Zealand: granitoid magmas formed by melting of mafic lithosphere. Journal of Geological Society, 152, 689-701.

Muir, R.J., Weaver, S.D., Bradshaw, J.D., Eby, G.N., Evans, J.A., 1995b. The Cretaceous Separation Point batholith, New Zealand: Granitoid magmas formed by melting of mafic lithosphere. Journal of the Geological Society, 152(4), 689-701.

Muntener, O., Kelemen, P.B., Grove, T.L., 2001. The role of H_2O during crystallization of primitive arc magmas under uppermost mantle conditions and genesis of igneous pyroxenites: an experimental study. Contributions to Mineralogy and Petrology, 141, 643-658.

Omrani, J., Agard, P., Whitechurch, H., Benoit, M., Prouteau, G., Jolivet, L., 2008. Arc magmatism and subduction history beneath the Zagros Mountains, Iran: a new report of adakites and geodynamic consequences. Lithos, 106, 380-398.

Omrani, J., Agard, P., Whitechurch, H., Benoit, M., Prouteau, G., Jolivet, L., 2009. Reply to: Comment by Aftabi and Atapour on "Arc magmatism and subduction history beneath the Zagros Mountains, Iran: A new report of adakites and geodynamic consequences". Lithos, 113, 847-849.

Ozdemir, Y., 2011. Volcanostratigraphy and petrogenesis of Suphan stratovolcano. Ph.D. Thesis. Ankara (Turkey), Middle East Technical University, 325 pp.

O'Neill, H.S.C., Palme, H., 1998. Composition of the silicate Earth: Implications for accretion and core formation. In: Jackson, I. (ed.). The Earth's Mantle: Structure, Composition, and Evolution—The Ringwood Volume. Cambridge, Cambridge University Press, 3-126.

Pang, K.N., Chung, S.L., Zarrinkoub, M.H., Hua Li, X., Yang Lee, H., Hsien Lin, T., Yi Chiu, H., 2016. New age and geochemical constraints on the origin of Quaternary adakite-like lavas in the Arabia-Eurasia collision zone. Lithos, 264, 348-359.

Patchett, P.J., Kuouvo, O., Hedge, C.E., Tatsumoto, M., 1981. Evolution of continental crust and mantle eterogeneity: evidence from Hf isotopes. Contributions to Mineralogy and Petrology, 78, 279-329.

Patchett, P.J., 1983. Importance of the Lu-Hf isotope system in studies of planetary chronology and chemical evolution. Geochimica et Cosmochimica Acta, 47, 81-91.

Pearce, J.A., Peate, D.W., 1995. Tectonic Implications of the Composition of Volcanic Arc Magmas. Annual Review of Earth and Planetary Sciences, 23, 251-285. DOI: doi.org/10.1146/annurev.ea.23.050195.001343

Petford, N., Atherton, M., 1996. Na-rich partial melts from newly underplated basaltic crust: the Cordillera Blanca Batholith, Peru. Journal of Petrology, 37, 1491-1521.

Prelevic, D., Akal, C., Foley, S.F., Romer, R.L., Stracke, A., Van Den Bogaard, P., 2012. Ultrapotassic mafic rocks as geochemical proxies for post-collisional dynamics of orogenic lithospheric mantle: the case of Southwestern Anatolia, Turkey. Journal of Petrology, 53, 1019-1055.

Qian, Q., Hermann, J., 2013. Partial melting of lower crust at 10–15kbar: Constraints on adakite and TTG formation. Contributions to Mineralogy and Petrology, 165(6), 1195-1224. DOI: 10.1007/s00410-013-0854-9

Rapp, R.P., Watson, E.B., 1995. Dehydration melting of metabasalt at 8–32kbar: implications for continental growth and crust-mantle recycling. Journal of Petrology, 36, 891-931.

Rapp, R.P., Shimizu, N., Norman, M., Applegate, G.S., 1999. Reaction between slab-derived melts and peridotite in the mantle wedge: experimental constraints at 3.8GPa. Chemical Geology, 160, 335-56.

Richards, J.R., Kerrich, R., 2007. Adakite-like rocks: their diverse origins and questionable role in metallogenesis. Economic Geology, 102, 537-576.

Richards, J.P., Boyce, A.J., Pringle, M.S., 2001. Geological evolution of the Escondida area, northern Chile: a model for spatial and temporal localization of porphyry Cu mineralization. Economic Geology, 96, 271-305.

Robin, C., Eissen, J.P., Samaniego, P., Martin, H., Hall, M., Cotten, J., 2009. Evolution of the late Pleistocene Mojanda–Fuya Fuya volcanic complex (Ecuador), by progressive adakitic involvement in mantle magma sources. Bulletin of Volcanology, 71(3), 233-258.

Rossetti, F., Nasrabady, M., Theye, T., Gerdes, A., Monie, P., Lucci, F., Vignaroli, G., 2014. Adakite differentiation and emplacement in a subduction channel: the late Paleocene Sabzvar magmatism (NE Iran). Geological Society of America Bulletin, 126, 317-343.

Rudnick, R.L., Gao, S., 2014. Composition of the Continental Crust. In: Holland, H.D., Turekian, K.K. (eds.). Oxford, Treatise on Geochemistry, Elsevier, 1-51.

Şengör, A., Özeren, S., Genç, T., Zor, E., 2003. East Anatolian high plateau as a mantle supported, north-south shortened domal structure. Geophysical Research Letters, 30, 1-24.

Shafaii Moghadam, H., Rosseti, F., Lucci, F., Chiaradia, M., Gerdes, A., Martinez Lopez, M., Ghorbani, Gh., Nasarabady, M., 2016. The calc–alkaline and adakitic volcanism of the Sabzevar structural zone (NE Iran): Implications for the Eocene magmatic flare–up in Central Iran. Lithos, 248-251, 517-535.

Shaker Aedakani, A., 2016. Post-collisional Plio-Pleistocene Anar-Dehaj adakitic subvolcanic cones in the central volcanic belt of Iran: geochemical characteristics and tectonic implications. Periodico di Mineralogia, 85, 185-200.

Shafaii Moghadam, H., Li Li, Q., Hua Li, X., Chiaradia, M., Karsli, O., Hoernle, K., Griffin, W., 2022. Mantle-derived high-K magmatic fluxes in northeast Iran arc: Constraints from zircon U-Pb-O-Hf and bulk rock major-trace elements and Sr-Nd-Pb isotopes. Gondwana Research, 119, 1-26. DOI: doi.org/10.1016/j.gr.2023.02.021

Söderlund, U., Patchett, P.J., Vervoort, J.D., Isachsen, C.E., 2004. The 176Lu decay constant determined by Lu–Hf and U-Pb isotope systematics of Precambrian mafic intrusions. Earth Planet Science Letters, 219, 311-324. DOI: https://doi.org/10.1016/S0012-821X(04)00012-3

Stevenson, R.K., Patchett, P.J., 1990. Implications for the evolution of continental crust from Hf isotope systematics of Archean detrital zircons. Gochimica et Cosmochimica Acta, 54, 1683-1697.

Streck, M.J., Leeman, W.P., Chesley, J., 2007. High-magnesian andesite from Mount Shasta: a product of magma mixing and contamination, not a primitive mantle melt. Geology, 35, 351-354.

Sun, S.S., McDonough, W.F., 1989. Chemical and isotopic systematic of oceanic basalts: Implication for mantle composition and processes. In: Saunders, A.D., Norry, M.J. (eds.). Magmatic in Oceanic Basins. London, The Geological Society, 42(Special Publications), 313-345.

Sun, W., Zhang, H., Ling, M.X., Ding, X., Chung, S.L., Zhou, J., Yang, X.Y., Fan, W., 2011. The genetic association of adakites and Cu–Au ore deposits. International Geology Review, 53, 691-703.

Sun, X., Lu, Y.J., McCuaig, T.C., Zheng, Y-Y., Chang, H.F., Guo, F., Li-Juan Xu, L., 2018. Miocene Ultrapotassic, High-Mg Dioritic, and Adakite-like Rocks from Zhunuo in Southern Tibet: Implications for Mantle Metasomatism and Porphyry Copper Mineralization in Collision. Journal of Petrology, 59(3), 341-386.

Topuz, G., Altherr, R., Schwarz, W.H., Siebel, W., Satır, M., Dokuz, A., 2005. Post-collisional plutonism with adakite-like signatures: the Eocene Saraycık granodiorite (Eastern Pontides, Turkey). Contributions to Mineralogy and Petrology, 150(4), 441-455

Verdel, C., Wernicke, B.P., Hassanzadeh, J., Guest, B., 2011. A Paleogene extensional arc flare-up in Iran. Tectonics, 30, 1-20.

Vervoort, J.D., Patchett, P.J., 1996. Behavior of hafnium and neodymium isotopes in the crust: constraints from Precambrian crustally derived granites. Geochimica et Cosmochimica Acta, 60(19), 3717-3733.

Wang, Q., Xu, J.F., Zhao, Z.H., Bao, Z.W., Xu, W., Xiong, X.I., 2004. Cretaceous high potassium intrusive rocks in the Yueshan-Hongzhen area of east China: adakites in an extensional tectonic regime within a continent. Chemical Geology, 38, 417-434.

Wang, Q., McDermott, F., Xu, J.-f., Bellon, H., Zhu, Y.-t., 2005. Cenozoic K-rich adakitic volcanic rocks in the Hohxil area, northern Tibet: lower-crustal melting in an intracontinental setting. Geology, 33(6), 465-468.

Wang, Q., Xu, J.F., Jian, P., Bao, Z.W., Zhao, Z.H., Li, C.F., Xiong, X.L., Ma, J.L., 2006a. Petrogenesis of adakitic porphyries in an extensional tectonic setting, Dexing, South China: Implications for the genesis of Porphyry Copper Mineralization. Journal of Petrology, 47, 119-144.

Wang, Q., Zhao, Z.H., Xu, J.F., Wyman, D., Xiong, X., Zi, F., Bai, Z., 2006b. Carboniferous adakite-high-Mg andesite-Nb enriched basaltic rock suites in the Northern Tianshan area: Implications for Phanerozoic crustal growth in the Central Asia Orogenic Belt and Cu-Au mineralization. Acta Petrologica Sinica, 22(1), 11-30.

Wang, Q., Wyman, D.A., Zhu, T., Feng, X., Zhang, Q., Zi, F., Chu, Z., 2008. Eocene melting of subducting continental crust and early uplifting of central Tibet: evidence from central-western Qiangtang high-K calc-alkaline andesites, dacites and rhyolites. Earth Planetary Science Letter, 272, 158-171.

Whitney, D.L., Evans, B.W., 2010. Abbreviations for names of rocks-forming minerals. American Mineralogist, 95, 185-187.

Winchester, J.A., Floyd, P.A., 1977. Geochemical discrimination of immobile elements. Chemical Geology, 20, 325-343.

Wu, F.Y., Yang, Y.H., Xie, L.W., 2006. Hf isotopic compositions of standard zircons and baddeleyites used in U-Pb geochronology. Chemical Geology, 231, 105-126.

Xu, J.F., Shinjo, R., Defant, M.J., Wang, Q., Rapp, R.P., 2002. Origin of Mesozoic adakitic intrusive rocks in the Ningzhen area of east China: Partial melting of delaminated lower continental crust? Geology, 30(12), 1111-1114.

Xu, H.J., Ma, C.Q., Ye, K., 2007a. Early Cretaceous granitoids and their implications for the collapse of the Dabie orogeny, eastern China: SHRIMP zircon U-Pb dating geochemistry. Chemical Geology, 240(3-4), 238-259.

Xu, Y.G., Wu, X.Y., Luo, Z.Y., Ma, J.L., Huang, X.L., Xie, L.W., 2007b. Zircon HF Isotope compositions of middle Jurassic-early Cretaceous intrusions in Shandong province and its implications. Acta Petrologica Sinica, 23(2), 307-316.

Xu, Y., Shen, S., Cai, Z., Zhou, G., 2008. The state of land subsidence and prediction approaches due to groundwater withdrawal in China. Natural Hazards, 45, 123-135.

Xu, J.F., Wu, J.B., Wang, Q., Chen, J.L., Cao, K., 2014. Research advances of adakites and adakitic rocks in China. Bulletin of Mineralogy Petrology & Geochemistry, 33, 6-13.

Yang, W.G., Zhong, Y., Zhu, L.D., Xie, L., Mai, Y.M., Li, N., Zhou, Y., Zhang, H.L., Xia Tong, X., Feng, W.N., 2022. The Early Cretaceous tectonic evolution of the Neo-Tethys: constraints from zircon U–Pb geochronology and geochemistry of the Liuqiong adakite, Gongga, Tibet. Geological Magazine, 159(10), 1-16.

Yogodzinski, G.M., Kelemen, P.B., 1998. Slab melting in the Aleutians: implications of an ion probe study of clinopyroxene in primitive adakite and basalt. Earth and Planetary Science Letters, 158, 53-65.

Yogodzinski, G.M., Kay, R.W., Volynets, O.N., Koloskov, A.V., Kay, S.M., 1995. Magnesian andesite in the west Aleutian Komandorsky region: implications for slab melting and processes in the mantle wedge. Geological Society of America Bulletin, 107, 505-519.

Yumul, G.P.Jr., Brown, W.W., Dimalanta, C.B., Ausa, C.A., Faustino-Eslava, D.V., Payot, B.D., Ramos, N.T., Lizada, A.N.L., Buena, A.E., Villaplaza, B.R.B., Manalo, P.C., Queaño, K.L., Guotana, J.M.R., Pacle, N.A.D., 2017. Adakitic Rocks in the Masara Gold-Silver Mine, Compostela Valley, Mindanao, Philippines: Different Places, Varying Mechanisms? Journal of Asian Earth Sciences, 142, 45-55. DOI: doi.org/10.1016/j.jseaes.2016.06.005.

Zhang, Q., Wang, Y., Qian, Q., Yang, J.H., Wang, Y.L., 2001. The characteristics and tectonicmetallogenic significances of the adakites in Yanshan period from eastern China. Acta Petrologica Sinica, 17, 236-244.

Zhang, H.F., Sun, M., Zhou, X.H., 2002. Mesozoic lithosphere destruction beneath the North China Craton: evidence from major- and trace-elements and Sr- Nd-Pb isotope studies of Fangcheng basalts. Contributions to Mineralogy and Petrology, 144, 241-253.

Zhang, Q., Jin, W.J., Li, C.D., Wang, Y.L., 2010. Revisiting the new classification of granitic rocks based on whole-rock Sr and Yb contents: Index. Acta Petrologica Sinica, 26, 985-1015.

Zhang, Q., Zhai, M.G., 2012. What is the Archean TTG? Acta Petrologica Sinica, 28, 3446-3456.

Zhang, L., Hu, Y., Liang, J., 2017. Adakitic rocks associated with the Shilu copper molybdenum deposit in the Yangchun Basin, south China, and their tectonic implications. Acta Geochimica, 36, 132-150.

Zhang, L., Shicho, L., Qingying, Z., 2019a. A review of research of adakites. International Geology Review, 63, 47-64.

Zhang, L., Li, S.H., Zhao, Q., 2019b. A review of research on adakites. International Geology Review, 63(6), 1-18. DOI: 10.1080/00206814.2019.1702592

Zheng, B., Yi-Gang, X., Griffin, W., Zhang, R.S., 2015. Are continental "adakites" derived from thickened or foundered lower crust? Earth and Planetary Science Letters, 419, 125-133.

Zhu, D.C., Zhao, Z.D., Pan, G.T., Lee, H.Y., Kang, Z.Q., Liao, Z.L., Wang, L.Q., Li, G.M., Dong, G.C., Liu, B., 2009. Early Cretaceous subduction-related adakite-like rocks of the Gangdese Belt, southern Tibet: Products of slab melting and subsequent melt-peridotite interaction? Journal of Asian Earth Sciences, 34, 298-309.

Zor, E., 2008. Tomographic evidence of slab detachment beneath eastern Turkey and the Caucasus. Geophysical Journal International, 175, 73-82.

Manuscript received May 2023;
revision accepted November 2023;
published Online January 2024.

APPENDIX I

TABLE I. Results of the zircon U–Pb geocronology analyses of samples CHE-2, CHE-3 and CHE-7 from the Chenar area

Spot	Concentration (ppm)				Measured Isotopic Ratios				Measured Isotopic Ages				
	U	Th	$^{207}Pb/^{206}Pb$	1s %	$^{207}Pb/^{235}U$	1s %	$^{206}Pb/^{238}U$	1s %	Rho	$^{207}Pb/^{235}U$	1s	$^{206}Pb/^{238}U$ Age	1s
CHE2-01	1038	742	0.0511	0.0052	0.006	0.001	0.0009	0.00002	0.224	6.4	0.6	5.8	0.1
CHE2-02	993	815	0.0461	0.0084	0.006	0.001	0.00092	0.00003	0.1846	6	1	5.9	0.2
CHE2-03	618	431	0.0472	0.0114	0.005	0.001	0.00082	0.00003	0.1535	5	1	5.3	0.2
CHE2-04	862	448	0.0576	0.0103	0.007	0.001	0.00082	0.00003	0.2111	7	1	5.3	0.2
CHE2-05	3891	9808	0.0487	0.0029	0.006	0.001	0.00084	0.00001	0.2045	5.7	0.3	5.4	0.1
CHE2-06	1432	1524	0.0477	0.0049	0.005	0.001	0.00083	0.00002	0.2401	5.5	0.6	5.3	0.1
CHE2-07	849	612	0.0467	0.0076	0.006	0.001	0.00086	0.00003	0.2196	5.6	0.9	5.5	0.2
CHE2-08	619	359	0.0526	0.0091	0.006	0.001	0.00083	0.00003	0.2127	6	1	5.3	0.2
CHE2-09	1198	1172	0.0507	0.0054	0.006	0.001	0.00086	0.00002	0.2243	6.1	0.6	5.5	0.1
CHE2-10	836	769	0.0533	0.0074	0.006	0.001	0.00086	0.00003	0.2594	6.4	0.9	5.5	0.2
CHE2-11	927	918	0.0474	0.0078	0.006	0.001	0.00091	0.00003	0.2019	6	1	5.9	0.2
CHE2-12	1642	2636	0.0491	0.006	0.006	0.001	0.00083	0.00003	0.3043	5.7	0.7	5.3	0.2
CHE2-13	825	1212	0.0603	0.0079	0.007	0.001	0.00084	0.00003	0.2837	7.1	0.9	5.4	0.2
CHE2-14	1126	888	0.059	0.006	0.007	0.001	0.00085	0.00002	0.2394	7	0.7	5.5	0.1
CHE2-15	598	321	0.0495	0.0092	0.006	0.001	0.00086	0.00003	0.1907	6	1	5.5	0.2
CHE2-16	556	320	0.0492	0.0103	0.006	0.001	0.00089	0.00004	0.22	6	1	5.7	0.3
CHE2-17	717	538	0.055	0.0089	0.006	0.001	0.00084	0.00003	0.2268	6	1	5.4	0.2
CHE2-18	835	804	0.0467	0.0069	0.006	0.001	0.0009	0.00002	0.154	5.9	0.8	5.8	0.1
CHE2-19	687	407	0.0561	0.0098	0.006	0.001	0.00083	0.00003	0.2119	7	1	5.3	0.2
CHE3-01	1130	1235	0.0631	0.0059	0.007	0.001	0.00083	0.00002	0.2688	7.3	0.7	5.3	0.1
CHE3-02	756	502	0.0472	0.0073	0.006	0.001	0.00085	0.00003	0.236	5.6	0.8	5.5	0.2
CHE3-03	4533	23022	0.1179	0.0045	0.014	0.001	0.00085	0.00001	0.3385	13.9	0.5	5.5	0.1
CHE3-04	369	180	0.0606	0.0135	0.007	0.002	0.00084	0.00004	0.2187	7	2	5.4	0.3
CHE3-05	429	275	0.0464	0.0113	0.005	0.001	0.00078	0.00003	0.161	5	1	5	0.2
CHE3-06	770	477	0.0578	0.0075	0.006	0.001	0.00079	0.00002	0.2016	6.4	0.8	5.1	0.1
CHE3-07	812	635	0.0774	0.0086	0.009	0.001	0.00084	0.00003	0.3389	9	0.9	5.4	0.2
CHE3-08	1084	1181	0.0539	0.005	0.007	0.001	0.00088	0.00002	0.2512	6.6	0.6	5.7	0.1
CHE3-09	795	731	0.0362	0.0061	0.004	0.001	0.00086	0.00002	0.1402	4.3	0.7	5.5	0.1
CHE3-10	738	536	0.0517	0.0062	0.006	0.001	0.0009	0.00002	0.188	6.5	0.8	5.8	0.1
CHE3-11	734	523	0.0481	0.0074	0.005	0.001	0.00082	0.00003	0.2414	5.5	0.8	5.3	0.2
CHE3-12	588	301	0.0533	0.0075	0.006	0.001	0.00085	0.00003	0.2569	6.3	0.9	5.5	0.2
CHE3-13	534	234	0.0517	0.0083	0.006	0.001	0.00084	0.00003	0.2244	6	1	5.4	0.2
CHE3-14	464	269	0.0619	0.0123	0.008	0.001	0.0009	0.00004	0.2291	8	1	5.8	0.3
CHE3-15	1041	627	0.0461	0.0054	0.005	0.001	0.00079	0.00003	0.3425	5.1	0.6	5.1	0.2
CHE3-16	1005	654	0.0474	0.0068	0.005	0.001	0.00083	0.00003	0.2554	5.5	0.8	5.3	0.2
CHE3-17	1059	1096	0.0504	0.005	0.006	0.001	0.00089	0.00002	0.2326	6.3	0.6	5.7	0.1
CHE3-18	582	304	0.0486	0.0085	0.006	0.001	0.00088	0.00003	0.1985	6	1	5.7	0.2

TABLE I. Continued

Spot	Concentration (ppm)		Measured Isotopic Ratios						Measured Isotopic Ages				
	U	Th	$^{207}Pb/^{206}Pb$	1s %	$^{207}Pb/^{235}U$	1s %	$^{206}Pb/^{238}U$	1s %	Rho	$^{207}Pb/^{235}U$	1s	$^{206}Pb/^{238}U$ Age	1s
CHE3-19	511	307	0.051	0.0105	0.006	0.001	0.00082	0.00003	0.1798	6	1	5.3	0.2
CHE3-20	1046	620	0.0508	0.0073	0.006	0.001	0.00079	0.00003	0.2692	5.6	0.8	5.1	0.2
CHE3-21	2926	5657	0.0681	0.0047	0.008	0.001	0.00088	0.00002	0.3533	8.3	0.5	5.7	0.1
CHE3-22	814	522	0.0537	0.0085	0.006	0.001	0.00083	0.00004	0.3182	6.2	0.9	5.3	0.3
CHE7-01	409	515	0.0744	0.008	0.009	0.001	0.00093	0.00003	0.3156	9.6	1	6	0.2
CHE7-02	1108	2278	0.0662	0.004	0.009	0.001	0.00098	0.00002	0.3641	9	0.5	6.3	0.1
CHE7-03	227	127	0.0546	0.0092	0.007	0.001	0.00088	0.00003	0.2061	7	1	5.7	0.2
CHE7-04	498	604	0.049	0.0046	0.007	0.001	0.00099	0.00002	0.2206	6.7	0.6	6.4	0.1
CHE7-05	3841	4712	0.051	0.0016	0.006	0.001	0.0008	0.00001	0.4147	5.7	0.2	5.2	0.1
CHE7-06	663	893	0.0544	0.004	0.007	0.001	0.00098	0.00002	0.2929	7.4	0.5	6.3	0.1
CHE7-07	259	129	0.0372	0.0071	0.005	0.001	0.00101	0.00003	0.1583	5.2	1	6.5	0.2
CHE7-08	335	285	0.0776	0.0063	0.014	0.001	0.00127	0.00003	0.3082	14	1	8.2	0.2
CHE7-09	187	108	0.0357	0.0088	0.005	0.001	0.00101	0.00004	0.162	5	1	6.5	0.3
CHE7-10	440	535	0.0509	0.0059	0.007	0.001	0.00102	0.00003	0.2629	7.2	0.8	6.6	0.2
CHE7-11	1188	1307	0.0621	0.0078	0.009	0.001	0.00103	0.00002	0.1568	9	1	6.6	0.1
CHE7-12	221	213	0.0539	0.0119	0.008	0.002	0.00104	0.00006	0.2696	8	2	6.7	0.4
CHE7-13	167	56	0.0479	0.0124	0.007	0.002	0.00113	0.00006	0.211	8	2	7.3	0.4
CHE7-14	447	320	0.0429	0.0068	0.006	0.001	0.00107	0.00004	0.2422	6.4	1	6.9	0.3
CHE7-15	348	291	0.055	0.0084	0.007	0.001	0.00099	0.00004	0.2751	8	1	6.4	0.3

TABLE II. Results of Lu-Hf isotope analyses of zircon grains from the Chenar area

Sample	Used Age	±1SE	$^{176}Yb/^{177}Hf$	±2SE	$^{176}Lu/^{177}Hf$	±2SE	$^{176}Hf/^{177}Hf$	±2SE	$^{178}Hf/^{177}Hf$	±2SE	$^{180}Hf/^{177}Hf$	±2SE	$(^{176}Hf/^{177}Hf)i$	$(^{176}Hf/^{177}Hf)1$ UCC Lu/Hf = 0.0093	$(^{176}Hf/^{177}Hf)2$ CC Lu/Hf = 0.015	$(^{176}Hf/^{177}Hf)3$ LCC Lu/Hf = 0.022	εHf(t)	±2SE	TDM CC
CHE-7-01	20.00	0.60	0.052044	0.002200	0.001547	0.000064	0.283122	0.000018	1.46724	0.00004	1.88690	0.00010	0.283121	0.283125	0.283127	0.283130	12.80	1.03	280.75
CHE-7-02	6.00	0.20	0.091729	0.006200	0.002315	0.000140	0.283124	0.000018	1.46718	0.00004	1.88685	0.00007	0.283124	0.283125	0.283125	0.283126	12.57	1.03	284.40
CHE-7-03	18.40	0.50	0.046549	0.000350	0.001086	0.000008	0.283016	0.000014	1.46722	0.00004	1.88710	0.00009	0.283016	0.283019	0.283021	0.283023	9.02	1.03	522.12
CHE-7-04	12.60	0.10	0.046202	0.002400	0.000918	0.000032	0.283031	0.000022	1.46722	0.00004	1.88716	0.00010	0.283031	0.283033	0.283034	0.283036	9.43	1.03	491.44
CHE-7-05	6.30	0.10	0.139237	0.002700	0.003976	0.000080	0.282858	0.000029	1.46703	0.00005	1.88679	0.00015	0.282858	0.282859	0.282859	0.282860	3.16	1.03	886.92
CHE-7-06	5.70	0.20	0.055815	0.002400	0.001184	0.000031	0.283039	0.000019	1.46712	0.00005	1.88694	0.00008	0.283039	0.283040	0.283040	0.283041	9.56	1.03	477.47
CHE-7-07	11.90	0.10	0.031996	0.001600	0.000742	0.000026	0.283041	0.000017	1.46716	0.00004	1.88730	0.00008	0.283041	0.283043	0.283044	0.283046	9.77	1.03	469.08
CHE-7-08	18.50	0.40	0.055045	0.000170	0.001288	0.000018	0.283095	0.000015	1.46720	0.00003	1.88705	0.00009	0.283095	0.283098	0.283100	0.283102	11.81	1.03	342.85
CHE-7-09	20.30	0.50	0.025571	0.000290	0.000675	0.000008	0.283097	0.000026	1.46715	0.00004	1.88701	0.00009	0.283097	0.283100	0.283102	0.283105	11.93	1.03	336.72
CHE-7-10	6.40	0.10	0.193479	0.002800	0.003993	0.000033	0.283073	0.000028	1.46717	0.00003	1.88696	0.00006	0.283073	0.283074	0.283074	0.283075	10.77	1.03	400.63
CHE-7-11	5.20	0.10	0.106720	0.001000	0.002083	0.000017	0.283044	0.000013	1.46720	0.00002	1.88698	0.00008	0.283044	0.283045	0.283045	0.283046	9.73	1.03	466.62
CHE-7-12	6.30	0.10	0.064649	0.001100	0.001405	0.000009	0.282984	0.000021	1.46715	0.00004	1.88700	0.00010	0.282984	0.282985	0.282986	0.282986	7.63	1.03	601.81
CHE-7-13	13.30	0.20	0.044884	0.001100	0.001000	0.000022	0.282948	0.000012	1.46719	0.00002	1.88693	0.00008	0.282948	0.282950	0.282951	0.282953	6.51	1.03	678.99
CHE-7-14	6.50	0.20	0.045777	0.003300	0.001047	0.000085	0.283060	0.000021	1.46722	0.00005	1.88714	0.00009	0.283060	0.283061	0.283062	0.283063	10.32	1.03	429.30
CHE-7-15	8.20	0.20	0.146649	0.004000	0.003232	0.000120	0.283092	0.000022	1.46719	0.00005	1.88701	0.00011	0.283092	0.283093	0.283094	0.283095	11.48	1.03	356.34
CHE2-01	5.80	0.10	0.025281	0.001700	0.000742	0.000049	0.283040	0.000015	1.46719	0.00003	1.88697	0.00006	0.283040	0.283041	0.283042	0.283042	9.60	1.03	475.04
CHE2-02	5.90	0.20	0.034629	0.002000	0.000903	0.000044	0.283022	0.000009	1.46717	0.00002	1.88696	0.00005	0.283022	0.283023	0.283024	0.283024	8.97	1.03	515.84
CHE2-03	6.20	0.50	0.019109	0.001000	0.000440	0.000024	0.283027	0.000017	1.46714	0.00003	1.88691	0.00008	0.283027	0.283028	0.283029	0.283029	9.15	1.03	504.20
CHE2-04	5.30	0.20	0.027417	0.002000	0.000735	0.000043	0.283060	0.000015	1.46720	0.00002	1.88678	0.00004	0.283060	0.283061	0.283061	0.283062	10.30	1.03	429.94
CHE2-05	5.30	0.20	0.051134	0.003500	0.001257	0.000072	0.283053	0.000011	1.46712	0.00003	1.88681	0.00004	0.283053	0.283054	0.283054	0.283055	10.05	1.03	445.95
CHE2-06	5.40	0.10	0.045160	0.001200	0.001087	0.000032	0.283001	0.000013	1.46713	0.00002	1.88685	0.00006	0.283001	0.283002	0.283002	0.283003	8.21	1.03	563.77
CHE2-07	5.30	0.10	0.036090	0.000730	0.000974	0.000027	0.282998	0.000015	1.46721	0.00003	1.88694	0.00004	0.282998	0.282999	0.282999	0.283000	8.11	1.03	570.59
CHE2-08	6.10	0.20	0.038203	0.002700	0.001059	0.000070	0.282999	0.000015	1.46710	0.00003	1.88681	0.00007	0.282999	0.283000	0.283001	0.283001	8.16	1.03	567.88
CHE2-09	5.50	0.20	0.030143	0.000720	0.000845	0.000018	0.282997	0.000012	1.46719	0.00002	1.88696	0.00007	0.282997	0.282998	0.282998	0.282999	8.07	1.03	572.71
CHE2-10	5.30	0.20	0.027949	0.000560	0.000807	0.000013	0.283014	0.000012	1.46721	0.00002	1.88697	0.00005	0.283014	0.283015	0.283015	0.283016	8.67	1.03	534.31
CHE2-11	5.50	0.10	0.021578	0.000480	0.000580	0.000015	0.283068	0.000017	1.46720	0.00002	1.88684	0.00006	0.283068	0.283069	0.283069	0.283070	10.59	1.03	411.62

TABLE II. Continued

Sample	Used Age	±1SE	$^{176}Yb/^{177}Hf$	±2SE	$^{176}Lu/^{177}Hf$	±2SE	$^{176}Hf/^{177}Hf$	±2SE	$^{178}Hf/^{177}Hf$	±2SE	$^{180}Hf/^{177}Hf$	±2SE	$(^{176}Hf/^{177}Hf)i$	$(^{176}Hf/^{177}Hf)1$ UCC Lu/Hf = 0.0093	$(^{176}Hf/^{177}Hf)2$ CC Lu/Hf = 0.015	$(^{176}Hf/^{177}Hf)3$ LCC Lu/Hf = 0.022	εHf(t)	±2SE	TDM CC
CHE2-12	5.50	0.20	0.023952	0.000770	0.000658	0.000016	0.282994	0.000013	1.46718	0.00002	1.88697	0.00005	0.282994	0.282995	0.282995	0.282996	7.97	1.03	579.46
CHE2-13	5.90	0.20	0.039200	0.001300	0.001059	0.000038	0.283036	0.000011	1.46719	0.00002	1.88691	0.00006	0.283036	0.283037	0.283038	0.283038	9.46	1.03	484.13
CHE2-14	5.30	0.20	0.080318	0.005300	0.001744	0.000120	0.283014	0.000013	1.46715	0.00002	1.88676	0.00005	0.283014	0.283015	0.283015	0.283016	8.67	1.03	534.52
CHE2-15	5.40	0.20	0.018756	0.001400	0.000530	0.000031	0.283035	0.000011	1.46726	0.00003	1.88705	0.00007	0.283035	0.283036	0.283036	0.283037	9.42	1.03	486.57
CHE3-01	5.30	0.10	0.038557	0.001100	0.001033	0.000038	0.283003	0.000011	1.46720	0.00003	1.88696	0.00005	0.283003	0.283004	0.283004	0.283005	8.28	1.03	559.28
CHE3-02	6.10	0.20	0.036867	0.000400	0.000930	0.000014	0.283042	0.000010	1.46720	0.00002	1.88697	0.00005	0.283042	0.283043	0.283044	0.283044	9.68	1.03	470.37
CHE3-03	5.50	0.20	0.041490	0.000910	0.001026	0.000020	0.283025	0.000011	1.46713	0.00003	1.88695	0.00007	0.283025	0.283026	0.283026	0.283027	9.06	1.03	509.30
CHE3-04	5.50	0.10	0.034047	0.000720	0.000895	0.000017	0.283023	0.000010	1.46720	0.00002	1.88687	0.00006	0.283023	0.283024	0.283024	0.283025	8.99	1.03	513.81
CHE3-05	5.40	0.30	0.026826	0.000320	0.000744	0.000015	0.283027	0.000014	1.46713	0.00003	1.88688	0.00004	0.283027	0.283028	0.283028	0.283029	9.13	1.03	504.76
CHE3-06	5.00	0.20	0.039664	0.002200	0.000916	0.000034	0.283006	0.000012	1.46717	0.00003	1.88695	0.00008	0.283006	0.283007	0.283007	0.283008	8.38	1.03	552.64
CHE3-07	5.10	0.10	0.026351	0.001400	0.000690	0.000031	0.283040	0.000012	1.46720	0.00002	1.88704	0.00005	0.283040	0.283041	0.283041	0.283042	9.59	1.03	475.45
CHE3-08	5.40	0.20	0.032543	0.001300	0.000868	0.000041	0.283011	0.000010	1.46713	0.00002	1.88689	0.00006	0.283011	0.283012	0.283012	0.283013	8.57	1.03	541.06
CHE3-09	5.70	0.10	0.056696	0.001100	0.001330	0.000034	0.283036	0.000012	1.46711	0.00002	1.88687	0.00004	0.283036	0.283037	0.283037	0.283038	9.46	1.03	484.31
CHE3-10	5.50	0.10	0.038302	0.001100	0.000994	0.000026	0.283043	0.000006	1.46720	0.00002	1.88691	0.00006	0.283043	0.283044	0.283044	0.283045	9.70	1.03	468.47
CHE3-11	5.80	0.10	0.032716	0.000700	0.000893	0.000015	0.283048	0.000010	1.46712	0.00002	1.88693	0.00006	0.283048	0.283049	0.283050	0.283050	9.88	1.03	456.92
CHE3-12	5.30	0.20	0.029087	0.000680	0.000813	0.000024	0.283024	0.000011	1.46721	0.00002	1.88699	0.00005	0.283024	0.283025	0.283025	0.283026	9.03	1.03	511.64
CHE3-13	5.50	0.20	0.028402	0.000710	0.000793	0.000020	0.283030	0.000012	1.46718	0.00003	1.88687	0.00007	0.283030	0.283031	0.283031	0.283032	9.24	1.03	497.91
CHE3-14	6.20	0.20	0.039722	0.000450	0.001010	0.000011	0.283027	0.000013	1.46718	0.00004	1.88684	0.00006	0.283027	0.283028	0.283029	0.283029	9.15	1.03	504.35
CHE3-15	5.40	0.20	0.038878	0.001100	0.001028	0.000033	0.283077	0.000009	1.46719	0.00003	1.88694	0.00007	0.283077	0.283078	0.283078	0.283079	10.90	1.03	391.33
CHE3-07	5.10	0.10	0.026351	0.001400	0.000690	0.000031	0.283040	0.000012	1.46720	0.00002	1.88704	0.00005	0.283040	0.283041	0.283041	0.283042	9.59	1.03	475.45
CHE3-08	5.40	0.20	0.032543	0.001300	0.000868	0.000041	0.283011	0.000010	1.46713	0.00002	1.88689	0.00006	0.283011	0.283012	0.283012	0.283013	8.57	1.03	541.06
CHE3-09	5.70	0.10	0.056696	0.001100	0.001330	0.000034	0.283036	0.000012	1.46711	0.00002	1.88687	0.00004	0.283036	0.283037	0.283037	0.283038	9.46	1.03	484.31
CHE3-10	5.50	0.10	0.038302	0.001100	0.000994	0.000026	0.283043	0.000006	1.46720	0.00002	1.88691	0.00006	0.283043	0.283044	0.283044	0.283045	9.70	1.03	468.47
CHE3-11	5.80	0.10	0.032716	0.000700	0.000893	0.000015	0.283048	0.000010	1.46712	0.00002	1.88693	0.00006	0.283048	0.283049	0.283050	0.283050	9.88	1.03	456.92
CHE3-12	5.30	0.20	0.029087	0.000680	0.000813	0.000024	0.283024	0.000011	1.46721	0.00002	1.88699	0.00005	0.283024	0.283025	0.283025	0.283026	9.03	1.03	511.64
CHE3-13	5.50	0.20	0.028402	0.000710	0.000793	0.000020	0.283030	0.000012	1.46718	0.00003	1.88687	0.00007	0.283030	0.283031	0.283031	0.283032	9.24	1.03	497.91
CHE3-14	6.20	0.20	0.039722	0.000450	0.001010	0.000011	0.283027	0.000013	1.46718	0.00004	1.88684	0.00006	0.283027	0.283028	0.283029	0.283029	9.15	1.03	504.35
CHE3-15	5.40	0.20	0.038878	0.001100	0.001028	0.000033	0.283077	0.000009	1.46719	0.00003	1.88694	0.00007	0.283077	0.283078	0.283078	0.283079	10.90	1.03	391.33